

Geophysical Monitoring of Geologic Sequestration in Aquifers and Depleted Oil and Gas Fields

MS Project Report
Department of Geophysics
Stanford University

David Wynn
August 2003

Abstract

The objective of this research is to explore the available options for monitoring a formation undergoing CO₂ injection. Rock physics models are used to determine the time-lapse changes in relevant physical properties (acoustic, electrical, etc.) for a variety of rock types at the pore scale. These rock physics models are used in a synthetic formation model to estimate field or measurement scale changes. Results from different settings are compared to suggest optimum monitoring techniques for monitoring geologic sequestration in brine aquifers and depleted oil and gas fields. Also examined are the potential uses of each technique for monitoring CO₂ migration, seal integrity, and mass balance. Seismic, electromagnetic, gravitational, and geodetic methods are the four broad types of subsurface geophysical monitoring examined. Two examples are used to illustrate the usefulness of this modeling approach: time-lapse seismic at Sleipner and deformation at Elk Hills.

Table of Contents

1. Introduction	1
1.1 Geologic Sequestration	1
1.2 Geophysical Monitoring	2
1.3 Formation Modeling	5
2. Seismic	7
2.1 Seismic Model	7
2.2 Lab Data Comparison	11
2.3 Field Scale Results	12
3. Electromagnetic	15
3.1 Electromagnetic Model	15
3.2 Field Scale Results	18
4. Gravity	20
4.1 Gravity Model	20
4.2 Field Scale Results	21
5. Deformation	23
5.1 Deformation Model	23
5.2 Field Scale Results	25
6. Sleipner Seismic	27
6.1 Geologic Setting	27
6.2 Sleipner Model	28
6.3 Field Scale Results	29
7. Elk Hills Deformation	31
7.1 Geologic Setting	31
7.2 Elk Hills Model	32
7.3 Field Scale Results	33
8. Conclusions	34
8.1 Summary of Results	34
8.2 Future work	35
Appendix A: Green's Function Derivation	36
References	38

1. Introduction

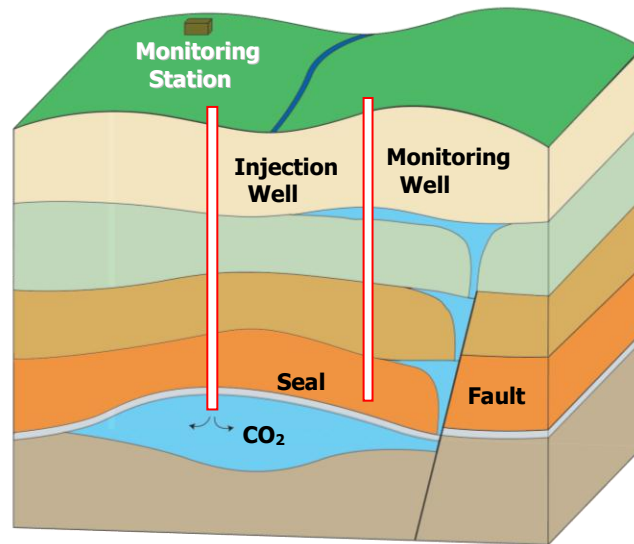


Figure 1.1—Schematic of CO₂ injection showing reservoir characteristics, injection geometry, and monitoring options.

1.1 Geologic Sequestration

CO₂ Sequestration is the process of capturing, separating, transporting, and storing waste CO₂. The motivation behind this process is that CO₂ is a greenhouse gas which is contributing to global climate change. By keeping the waste gas from escaping to the atmosphere, it is hoped that this greenhouse effect can be mitigated. Of the three principal types of sequestration being considered, namely geologic, oceanic, and terrestrial, geologic sequestration seems to offer the most feasible solution in the short term. While reforestation takes time and oceanic injection is meeting resistance from environmental groups, subsurface CO₂ injection, though not a new concept, has the potential to provide near term economic benefits.

For decades the petroleum industry has used CO₂ for enhanced oil recovery (EOR) as a secondary recovery technique, injecting CO₂ to increase oil production, sometimes dramatically. In 1998 an average of 0.76 million barrels per day were produced in the U.S. through EOR, or 12% of the total produced, about 23% of that using CO₂ (Mortis, 1998). This process has been limited primarily by the availability of CO₂ and has been confined mostly to the West Texas and New Mexico Permian basin using natural sources of CO₂ (Orr, 1984); with an abundance of concentrated CO₂ available for injection this process would certainly be used on a wider basis and the additional profit in oil production would help offset the cost of sequestration.

Three options being considered for geologic sequestration are deep unminable coal seams,

depleted oil and gas reservoirs, and deep saline aquifers. While coal seams are an attractive option for enhanced coalbed methane production (ECBM), the physical and chemical behavior of coal is still poorly understood. For this reason the latter two options will be the focus of this research. From a rock physics standpoint aquifers and depleted oil and gas fields differ only in the composition of their pore fluid, though that difference in itself may have a dramatic effect on the usefulness of a particular monitoring technology. Fig. 1.1 shows some of the monitoring options for and important formation characteristics of geologic sequestration.

CO₂ has a critical temperature of 31 °C and a critical pressure of 7.4 MPa. Below about 800 meters in depth CO₂ injected into the subsurface under typical geothermal conditions with near hydrostatic pressures will exist in a supercritical state. In this state CO₂ has gas-like compressibility, viscosity, and surface tension with liquid-like densities (~0.5 g/cc). The effect of the low viscosity and surface tension is that CO₂ will flow easily into a reservoir but that leakage through faults or other features will allow for CO₂ to escape more easily than a less viscous fluid would. Interpolated data from Wang (1989) and Vargaftik (1996) is used to obtain these quantities for modeling CO₂ behavior under specific reservoir conditions. Additionally, supercritical CO₂ is immiscible and soluble in water, and is nonconductive.

Injecting CO₂ in a supercritical state has several advantages in terms of storage. Due to its high density there will be less pressure buildup associated with gas columns and more storage per unit volume. Though dense, in most circumstances CO₂ will be buoyant in reservoir oil and brine, meaning that it will be contained in existing structural traps, in the absence of leakage, until it is eventually trapped for geologic periods of time. The short-term structural trapping is commonly called hydrodynamic trapping, and the long-term trapping may take the form of solubility trapping or mineral trapping (Houghton, 1999). Solubility trapping the process by which CO₂ is dissolved in the formation fluids, increasing their density and removing the gravity drive. Mineral trapping, on the other hand, involves converting the CO₂ to a solid mineral form through geochemical reactions.

1.2 Geophysical Monitoring

The motivation for monitoring is threefold: process efficiency, storage verification, and safety. The process of injecting CO₂ into the subsurface is analogous to that of enhanced oil production. In both cases it is important to know which areas of the formation are being contacted in order to efficiently develop a site, thus it is necessary that we be able to track the movement or migration of injected CO₂. Also, as CO₂ is denser than air at atmospheric conditions and is an asphyxiant, there is concern for public safety should leakage occur through a conduit to the surface. To address this concern we need to

monitor leakage and cap rock integrity. Finally, as the goal of sequestration is ultimately to store CO₂ in the subsurface it is also important that its containment and trapping be verified; to achieve this we require a mass balance. To summarize, one would like to monitor, in order of importance: CO₂ migration for process efficiency, seal integrity for public safety, and mass balance for storage verification.

There are a wide range of monitoring techniques available to meet these needs. These methods range from spaceborne satellites to surface stations to borehole devices. The two general options for monitoring are direct and remote sensing methods. Direct sampling methods have high spatial resolution but low spatial coverage; examples of these are surface chemical sensors and monitoring wells. The techniques discussed in this work are subsurface geophysical imaging techniques which generally have high spatial coverage but low spatial resolution. These are divided into seismic, electromagnetic, gravitational, and geodetic techniques. Geophysical methods have the added benefit of being remote. While a monitoring well would have to penetrate the formation seal to gather meaningful hydrologic data or fluid samples, possibly creating conduits for CO₂ to escape, geophysics may be used to image the area of interest without such intrusion.

In examining the three monitoring goals stated above, it is evident that none of these goals may be wholly achieved without the aid of geophysics, nor will geophysics alone provide the solution we need. High spatial coverage will be necessary to assess CO₂ movement and storage, coverage which monitoring wells alone will be unable to provide. That is not to say that direct methods will not be useful, a combination of direct and remote techniques will certainly be necessary to effectively monitor sequestration. Individual geophysical techniques and their uses and applications will be examined below for each of the four broad types of subsurface monitoring for the range of formation types.

Used for time-lapse monitoring, these geophysical methods can be very powerful. As opposed to the use of geophysics for characterization, where the subsurface geology is unknown, time-lapse monitoring is only carried out after extensive characterization has been carried out in baseline surveys. Repeatability then becomes an important issue which may be solved through the use of fixed measurement devices either on the surface or in the subsurface. The benefit of time-lapse monitoring is that some effects, such as lithology and cementation, are removed as they are assumed to remain constant between surveys (Wawersik, 2001). The change is then associated only with changes in the pore fluid composition and pore pressure. Most of the research occurring in this area has been in seismic reflection and tomography, while geodetic techniques, also time-lapse, have seen less use in subsurface monitoring.

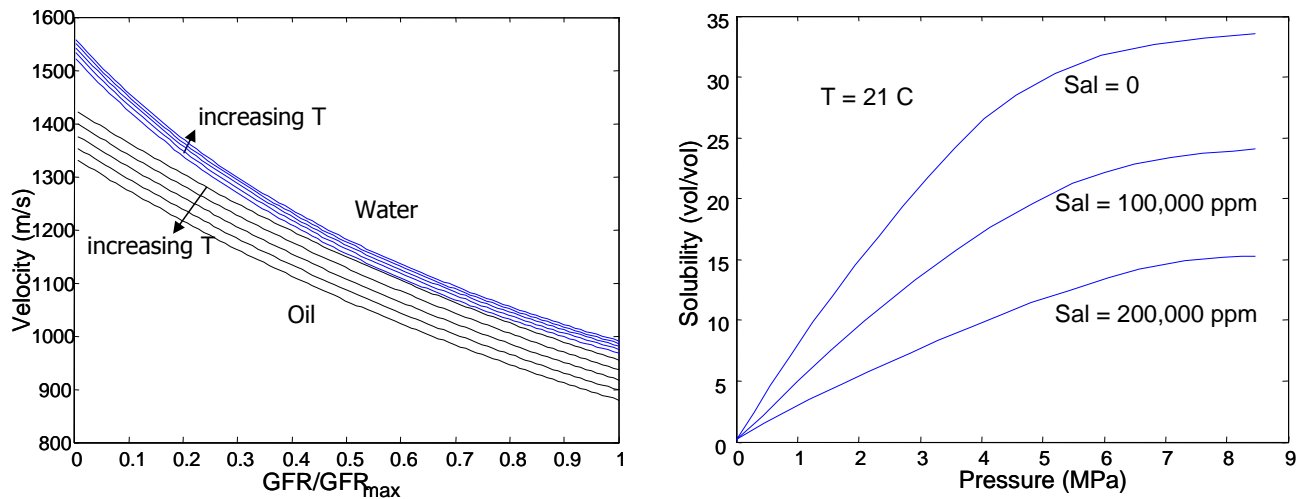


Figure 1.2—(a) Water and oil properties as a function of increasing CO₂ content using Batzle and Wang's relations and (b) CO₂ solubility in brine (Latil, 1980).

The most significant changes in the properties of the rocks and fluids in a formation undergoing CO₂ injection are expected to result from saturation and pressure changes. Changes in R_{CO_2} , the CO₂ fluid ratio, be the fluid oil or brine, are expected to produce only minor changes in the fluid properties as will be shown below. This assertion is made with the assumption that injection is approximately isothermal and that any significant geochemical changes will occur on a longer time scale than is of interest from a monitoring standpoint.

Pressure and saturation changes may have a dramatic effect on the bulk properties of the fluid. Increasing CO₂ saturation will cause the bulk fluid density and viscosity to decrease, while the effective compressibility will be dramatically increased. Brine conductivity is treated as a constant as the water salinity is assumed to have reached an equilibrium state. Isostress mixing is assumed in the modeling; mixing of the fluids in the pore space is assumed to occur at the finest scale. Changes in the pore fluid and pore pressure bring about a host of changes in the effective properties of the saturated rocks which may be detected through the use of remote sensing techniques. The specific changes will be addressed individually, but in general there are changes in the physical, acoustic, and electrical properties, ranging from few percent changes in seismic velocity to order of magnitude changes in rock conductivity.

Changes in R_{CO_2} will be ignored in this study for two reasons. First, the magnitude of the changes in fluid properties resulting from CO₂ dissolution are of a lower order of magnitude than the those associated with saturation changes. Second, changes in R_{CO_2} will occur on a different timescale than injection. Modeling changes in R_{CO_2} will, however, certainly be important for long-term monitoring simulations; it's effects on the thermodynamic properties of reservoir fluids can be approximated to the first order with the Batzle and Wang (1992) relations by using the specific weight

of CO₂ in place of hydrocarbon gas. The set of relations underpredict the amount of CO₂ that can be dissolved in brines (Fig. 1.2b), but fit the behavior of reservoir fluids with dissolved CO₂ well for a given gas fluid ratio. Fig. 1.2a shows the effect of increasing CO₂ saturation in oil and water. At maximum saturation velocities decrease by approximately 30%, while the velocity decrease resulting from the mixing of CO₂ with these fluids is much greater.

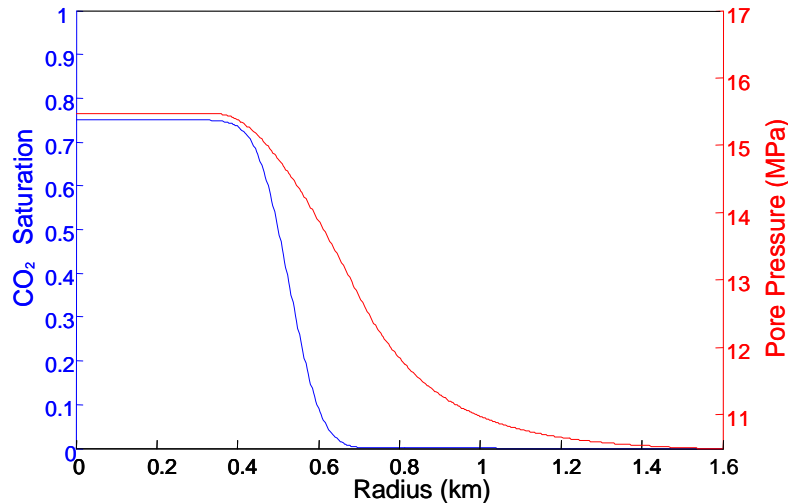


Figure 1.3—Radial profile of saturation and pressure at constant depth. The pressure is communicated beyond the saturation front.

1.3 Formation Modeling

The four broad subsurface imaging techniques will be examined separately. Each contains a discussion of how the relevant fluid properties change with pressure and CO₂ saturation. This fluid model is then incorporated into a rock physics model which is dependent on both rock type and pore fluid. Finally each of the rock physics models is applied to a reservoir model to produce field scale changes which are compared for the settings of interest. The reservoir model is or a cylindrically symmetric tabular reservoir 100 meters thick with a vertical injection well at its center. Injection is at a constant mass rate of 1.5 million tons per year of CO₂, and results are displayed after 10 years of injection. The geometry seen in Fig. 1.4 and other similar figures is a reservoir cross-section with the vertical injection well at the left edge of the figure.

The three aspects of CO₂ front behavior that the injection model attempts to capture are gravity segregation, mixing at the saturation front, pressure front behavior. As can be seen in Fig. 1.4a the bubble geometry is driven by gravity segregation resulting from the differences in fluid densities. Under most formation conditions CO₂ will be lighter than the fluid in-place, resulting in a vertical gravity drive. Fig. 1.4b shows the pore pressure in the reservoir which is a combination of hydrostatic background pressure with a perturbation from injection pressure varying with radial distance from the

well. The saturation curve shown in Fig. 1.3 is approximately the expected shape associated with stable miscible fluid displacement, such as would be expected in a depleted oil reservoir above the minimum miscibility pressure (MMP). Also displayed in Fig. 1.3 is a pressure profile. The model has a linearly increasing injection pressure which is communicated equally throughout the CO₂ saturated region. Pressure falls off smoothly through the mixed region, transitioning into a gradual exponential integral decay extending out into the unsaturated region.

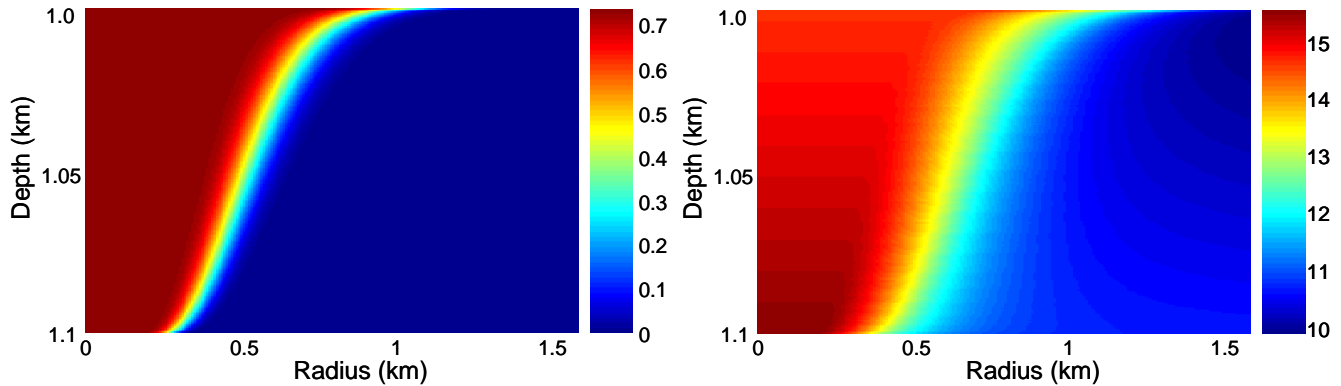


Figure 1.4—(a) CO₂ saturation and (b) formation pore pressure in MPa as a function of depth and radius after 10 years of simulated injection.

The injection model is meant to qualitatively capture the behavior of a CO₂ front, not to be a rigorous reservoir simulation. The model is used as a test case for the geophysical tools and models presented in this research. This model is idealized as it describes an isotropic homogenous system which is never the case in the real world. Any realistic flow would have viscous fingering associated with heterogeneity in both the rocks and fluids, and viscous instability, where CO₂ will seek the easiest flow path (Orr, 1984). Miscible flow can have the effect of stabilizing the saturation front, but in immiscible displacement, such as would occur below the MMP or in an aquifer, an unstable front will develop (Wang, 1982).

2. Seismic

In seismic monitoring the changes we may detect are changes in velocity, reflectivity, and possibly attenuation. Attenuation will be briefly discussed qualitatively while the velocity and reflectivity will be discussed in more detail. The models we use to describe the seismic properties of formation rocks undergoing CO₂ injection are Gassmann fluid substitution and Eberhart-Phillips stress-dependence. In general, the changes in seismic properties are a result of saturation changes and changes in the effective stress. After developing the necessary models we will compare our modeling results to published data.

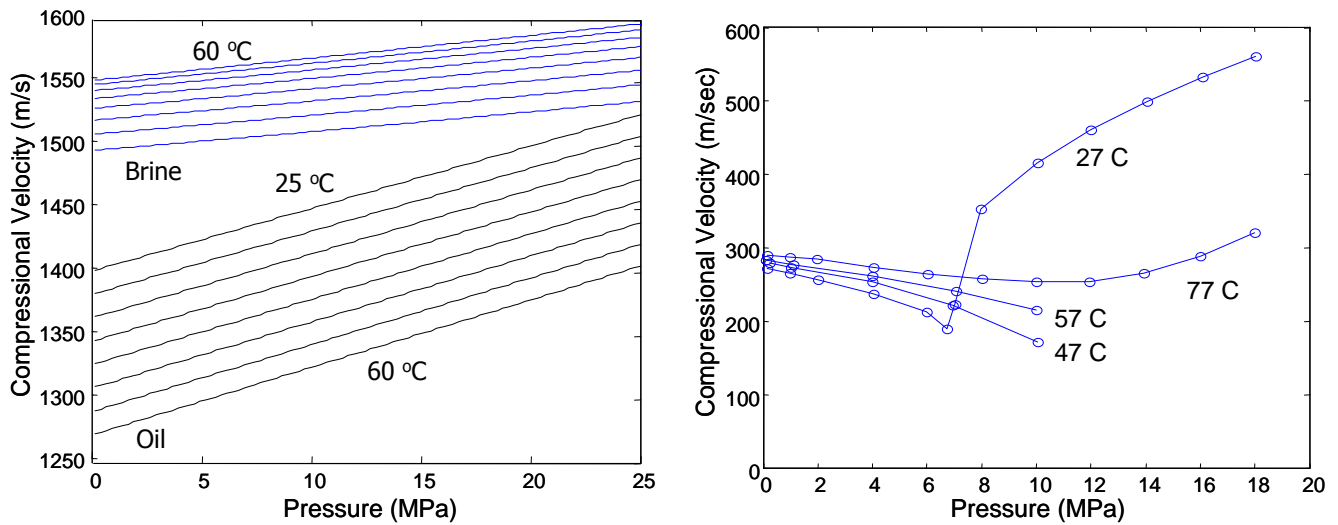


Figure 2.1—Compressional velocities in (a) brine and oil, and (b) CO₂ as a function of pressure and temperature.

2.1 Seismic Model

The seismic properties of the pore fluids that we're concerned with are density and the bulk modulus. The properties of the brine and oil initially present in the formation are fairly insensitive to reservoir conditions while the seismic properties of CO₂ are much stronger functions of pressure and temperature (Fig. 2.1). We use the relations collected by Batzle and Wang (1992) to estimate the seismic properties of oil, brine, and hydrocarbon gas. Isostress mixing is assumed for the pore fluids, which leads us to the following effective fluid properties for density and bulk modulus:

$$\rho_{\text{eff}} = \sum_i f_i \rho_i \quad \text{and} \quad \frac{1}{K_{\text{eff}}} = \sum_i \frac{f_i}{K_i} \quad (2.1)$$

In these expressions f is the volume fraction of fluid i , ρ is fluid density, and K is the bulk modulus of the fluid. As mentioned previously, changes in R_{CO_2} will affect on the seismic properties of brine and oil, but will be a secondary effect to saturation and pressure changes and will also be dependent on the

time-scale of CO₂ dissolution.

Gassmann's fluid substitution is a low frequency theory which allows one to determine the effect of pore fluid changes on rock moduli. Using the above effective fluid properties in Gassmann's equation along with the mineral modulus and the dry rock modulus, one can solve for the saturated moduli with

$$\frac{K_{sat}}{K_0 - K_{sat}} = \frac{K_{dry}}{K_0 - K_{dry}} + \frac{K_{fl}}{\phi(K_0 - K_{fl})} \quad \text{and} \quad \mu_{dry} = \mu_{sat} \quad (2.2)$$

where K_0 , K_{dry} , and K_{sat} are the mineral, dry rock, and saturated bulk moduli respectively. ϕ is the porosity and μ is the shear modulus which is unchanged upon fluid substitution under Gassmann's theory. The saturated density also changes as a result of changing the pore fluid, and can also be calculated from

$$\rho_{sat} = \phi\rho_{fl} + \rho_{dry} \quad (2.3)$$

The two materials making up the mineral of our shaly sandstone are quartz and clay. To find the mineral modulus of sandstone rocks we will use the Hashin-Shtrikman upper and lower bounds

$$K^{HS \pm} = K_1 + \frac{f_2}{(K_2 - K_1)^{-1} + f_1(K_1 + \frac{1}{3}\mu_1)^{-1}} \quad (2.4)$$

The two bounds are found by simply changing which component is labeled 1 and 2. As the bounds are fairly tight for clay and quartz, we will use the average of the two for our mineral modulus. To find the dry density of our composite rock we can use

$$\rho_{dry} = (1 - \phi)(C\rho_C + (1 - C)\rho_Q) \quad (2.5)$$

where the subscripts Q and C represent quartz and clay mineral density respectively and C is the mineral fraction of clay. Clay content also plays an important role in the stress-dependence of seismic properties.

To model the stress-dependence of fractured rocks we use the results of Eberhart-Phillips (1989). His work is based on data gathered by Han (1986) on the stress-dependent velocities of 64 sandstone samples. In practice stress-dependence will need to be determined as part of site specific characterization. Eberhart-Phillips used only sandstone data, but a similar stress-dependence may occur in fractured carbonates. He found the following empirical relation for compressional and shear velocity as a function of porosity, clay content, and effective pressure:

$$V_p = 5.77 - 6.94\phi - 1.73\sqrt{C} + 0.446(P_e - e^{-16.7P_e}) \quad (2.6a)$$

$$V_s = 3.70 - 4.94\phi - 1.57\sqrt{C} + 0.361(P_e - e^{-16.7P_e}) \quad (2.6b)$$

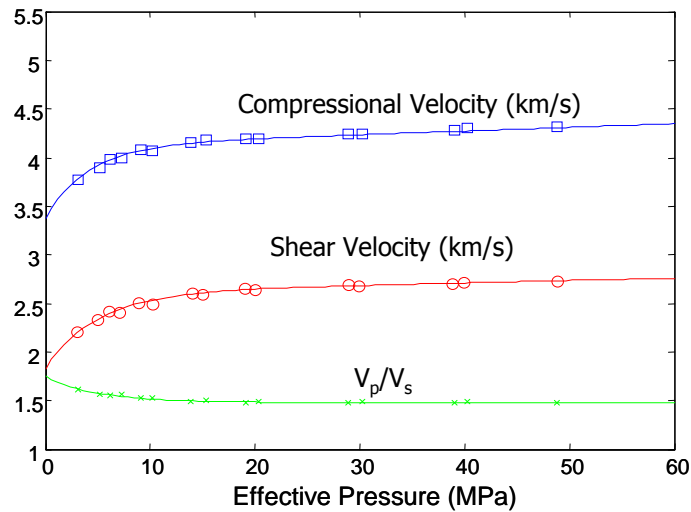


Figure 2.2—Data from Eberhart-Phillips (1989) for the StPeter1 sample.

In these two expressions, P_e is the effective pressure is in kbar and V_p and V_s are in km/s. Note that the exponential term involving the effective pressure is independent of porosity and clay content. This is due to the fact that the exponential behavior at low effective pressures could not be fit using clay content and porosity, not because all of the sample rocks displayed the same dependence on effective pressure. Fig. 2.2 illustrates the effect of changing effective stress on a particular sample, StPeter1. These data were collected for water-saturated rocks; the saturated moduli may then be found from the well-known dependence of velocity on elastic moduli and density (Eq. 2.7).

Combining Gassmann and Eberhart-Phillips allows one to predict the changes from increasing pore pressure and changing saturation with injection and compare the two effects as will be done below. Fig. 2.3 and Fig. 2.4 displays the results of numerical experiments on a stress dependent sandstone and a stiffer, unfractured carbonate undergoing CO₂ flooding. The top curve in each plot is strait Gassmann, while each of the other curves assumes a linear increase in pressure with CO₂ saturation. Each curve begins at the same reference pore pressure and at zero CO₂ saturation. The first thing to notice is that the stiffer rock has a much smaller percent change in velocity, meaning that any changes will be much harder to detect. Also important is that in the fractured sandstone approximately half of the compressional velocity change results from saturating changes and half from pressure effects, while the shear velocity is more affected by pressure changes, which agrees with published results (Wang, 1998).

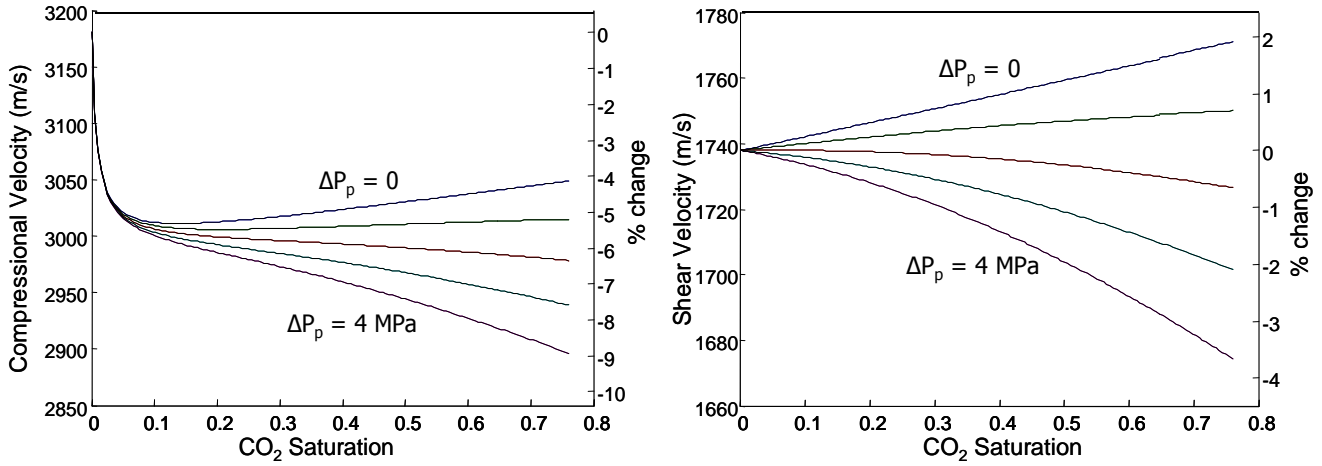


Figure 2.3—Calculated (a) compressional and (b) shear velocities with CO₂ flooding using Gassmann fluid substitution and sandstone stress-dependence.

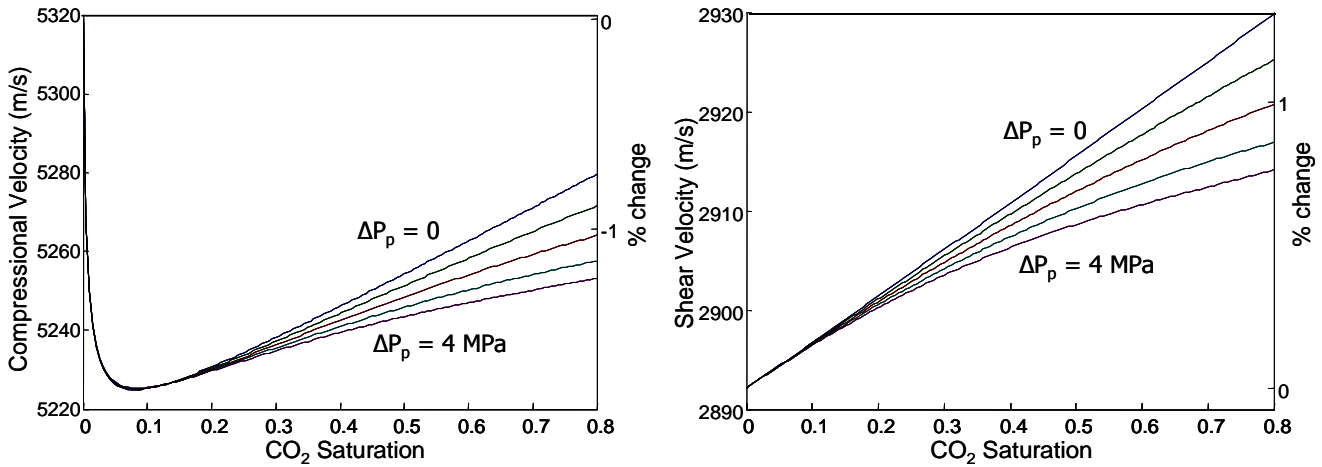


Figure 2.4—Calculated (a) compressional and (b) shear velocities with CO₂ flooding using Gassmann fluid substitution for a stiff unfractured rock with no stress-dependence.

Using the saturated moduli and Gassmann we may extract the dry moduli which may then be used, along with predicted saturations from flow modeling, to estimate the saturated moduli. Transforming these moduli back to velocity we can predict the formation velocities using

$$v_p = \sqrt{\frac{K + \frac{4}{3}\mu}{\rho}} \quad \text{and} \quad v_s = \sqrt{\frac{\mu}{\rho}} \quad (2.7)$$

To upscale this to what we expect to see at the field scale in a seismic reflection survey we find the seismic impedance and generate a reflectivity series. This process will be examined in more detail in the seismic results section. Calculating the impedance is straightforward and is simple the product of the local density and velocity

$$Z_i = \rho V_i \quad (2.8)$$

This expression is true for both compressional and shear waves. For the purpose of creating synthetic

reflection data, our model is divided into discrete pixels with a single pressure, velocity, and density. Reflectivity between pixels is then easily found from the impedances of the upper and lower pixels using

$$R = \frac{Z_2 - Z_1}{Z_2 + Z_1} \quad (2.9)$$

The next step is to take this reflectivity image in space and use the velocities to convert it to a reflectivity time series with interval spacing matching the time sampling of our source wavelet. For this we use a Ricker wavelet to approximate the signal generated by a seismic source.

There will also be changes in seismic attenuation as a result of CO₂ injection. Quantitative prediction of these changes may not be possible with current models, but qualitative changes may be tested. The attenuation coefficient is approximately given for fast shear and compressional waves by

$$\alpha \sim \frac{\omega^2 k}{v\rho} \left(\frac{\rho_f}{\eta} \right) \quad (2.10)$$

(Berryman, 1988). Here ω is the frequency of the seismic wave, ρ is the bulk density, ρ_f is the fluid density, η is the effective viscosity, k is the permeability, and v is the seismic velocity. At typical reservoir condition, CO₂ flooding will change the fluid density and rock velocity by up to ten percent, while the viscosity can vary by up to an order of magnitude depending on how one computes the effective fluid behavior. The resonant frequencies of the rocks will also change with flooding, and their dependence on fluid properties can be described by

$$\omega_0 \sim \frac{\eta}{\rho_f} \quad \text{and} \quad \omega_0 \sim \frac{K_f}{\eta} \quad (2.11)$$

(Pride, 2003). The first resonant frequency applies to Biot attenuation, while the second applies to squirt type mechanisms. Measuring this effect in the field would require broadband measurement and be financially prohibitive from a monitoring standpoint.

2.2 Lab Data Comparison

Wang and Nur (1989) conducted laboratory experiments on sandstone samples under hydrocarbon saturated and CO₂ flooded saturations. The samples were initially saturated with n-hexadecane then flooded with CO₂ leaving approximately 30% residual oil. The confining stress was kept constant at 20 MPa while the pore pressure was increased from approximately 0 to 18 MPa. The results for the Beaver No. 7 sample are shown in Fig. 2.5a. Fig. 2.5b shows the simulated results from our model.

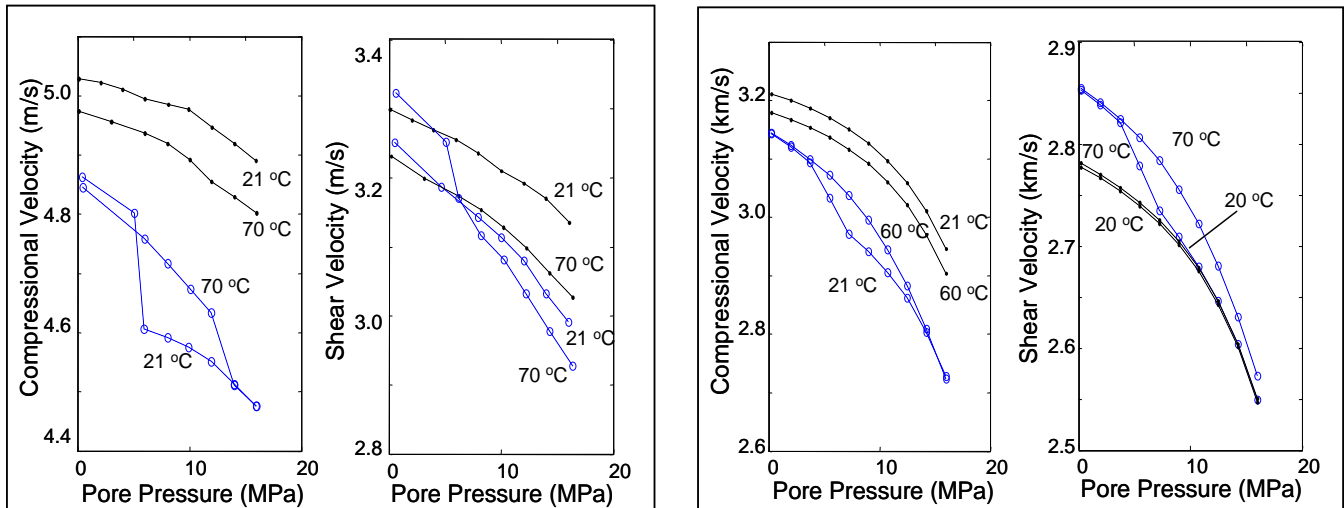


Figure 2.5—A comparison between (a) lab data from Wang (1989), Beaver No. 7 and (b) our stress-dependent fluid substitution model. Black lines are isotherms for hydrocarbon saturated rocks and blue lines are isotherms for flooded rocks. Confining pressure for all plots is 20 MPa.

The compressional velocities display similar qualitative behavior while the shear velocities exhibit some striking differences. From Gassmann we predict that the shear modulus is unchanged upon flooding, and any velocity change will be the result of density changes. As less dense CO_2 is displacing hydrocarbon oil we expect that flooding will always increase shear velocity. The unexpected behavior of the shear velocity curves in the lab data can be attributed to high frequency viscous effects; Gassmann is a zero frequency equation and cannot always describe sample behavior at laboratory frequencies. Measurements made at field frequencies are expected to show more Gassmann like behavior.

2.3 Field Scale Results

Figs. 2.6 and 2.7 display the seismic property changes resulting from our simple injection model. Note that just as we saw in our rock physics models, V_p show the effects of both saturation and pressure changes, while V_s more clearly tracks the pressure front. Using these results and Eqs. 2.8 and 2.9 we are able to create impedance and reflectivity images for our model (Figs. 2.9 and 2.10). Using this reflectivity time-series and our source wavelet in a convolutional model we can create synthetic seismic reflection images of our model. In these images we can clearly see the reflector pull-down (Fig. 2.9b) from the lower velocities in the CO_2 saturated region and the bright spot associated with the presence of CO_2 (Fig. 2.9c).

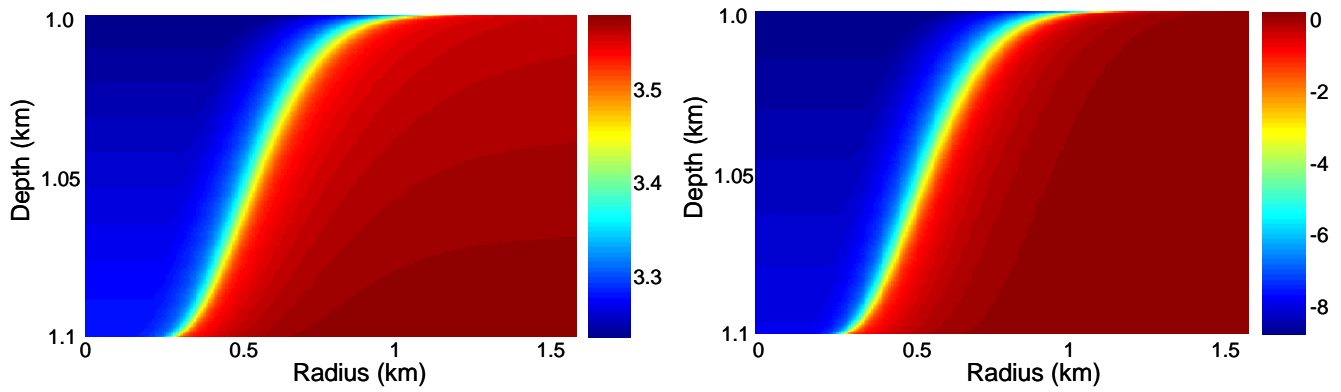


Figure 2.6—(a) Compressional velocity in km/s and (b) percent change in compressional velocity.

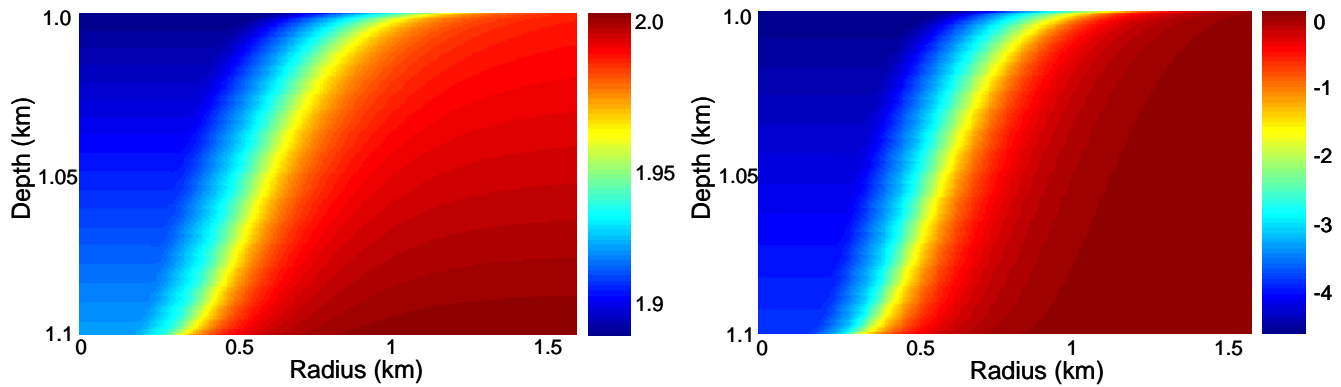


Figure 2.7—(a) Shear velocity in km/s and (b) percent change in shear velocity.

Three of the principal seismic methods being considered for monitoring sequestration are reflection seismic, velocity tomography, and microseismic. Reflection seismic and crosswell tomography are both expensive, high resolution techniques. Crosswell seismic imaging techniques have been employed before to monitor CO₂ injection in EOR at the McElroy Field in West Texas. The seismic survey and the accompanying rock physics study showed that a several percent change was both present and detectable (Lazaratos, 1997; Nolen-Hoeksema, 1995; Wang 1998) using tomographic techniques.

Another option available is microseismic monitoring. This technique involves using fixed continuous geophones to monitor a formation, providing a real-time image of CO₂ movement. This is a relatively inexpensive passive technique which detects elastic waves resulting from fracture formation or reopening. Fracture formation is, in turn, strongly dependent on pressure changes, so it may only be useful in low permeability, low porosity rocks where significant pressure changes are expected to occur (SACS, 2003).

From the rock physics modeling discussed previously (Fig. 2.3), the bulk of the velocity changes resulting from saturation effects occur with only a small amount of CO₂ in the pore space. This means that differentiating 20% saturation from 60% saturation will be much more difficult than detecting the

presence of CO₂. For this reason the principal usefulness of seismic monitoring will be in leak detection and for monitoring CO₂ migration rather than mass balance. Seismic should be able to detect thin layers of CO₂ (McKenna, 2003), meaning that migration paths should show up clearly in a reflection survey and that presence of CO₂ in overlying aquifers should be easily detectable.

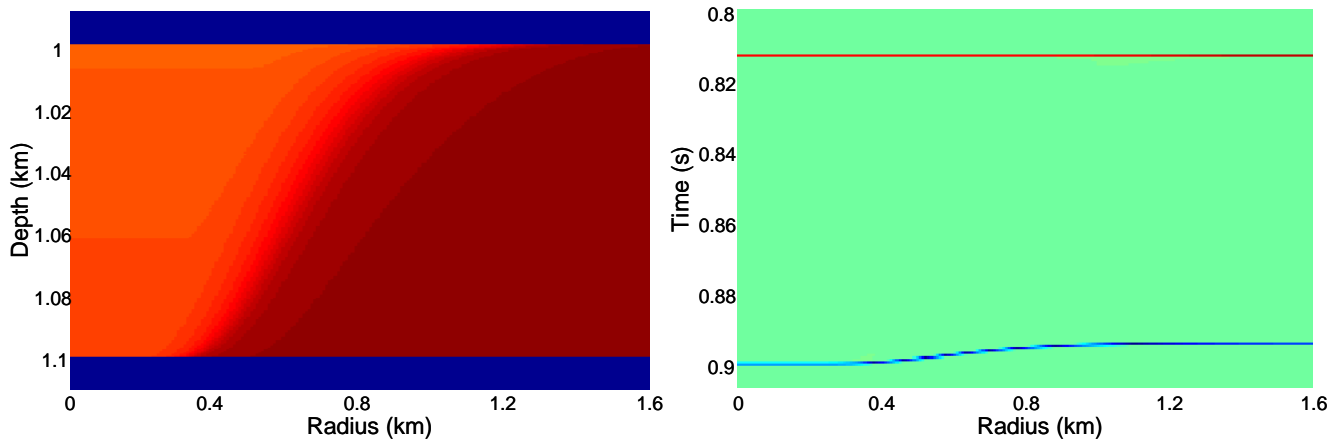


Figure 2.8—Compressional impedance image (a) of the reservoir with the bounding shale layers. In this case the only significant and detectable contrasts appear at the sand shale interface. (b) Reflectivity series in time for our injection model after 10 years

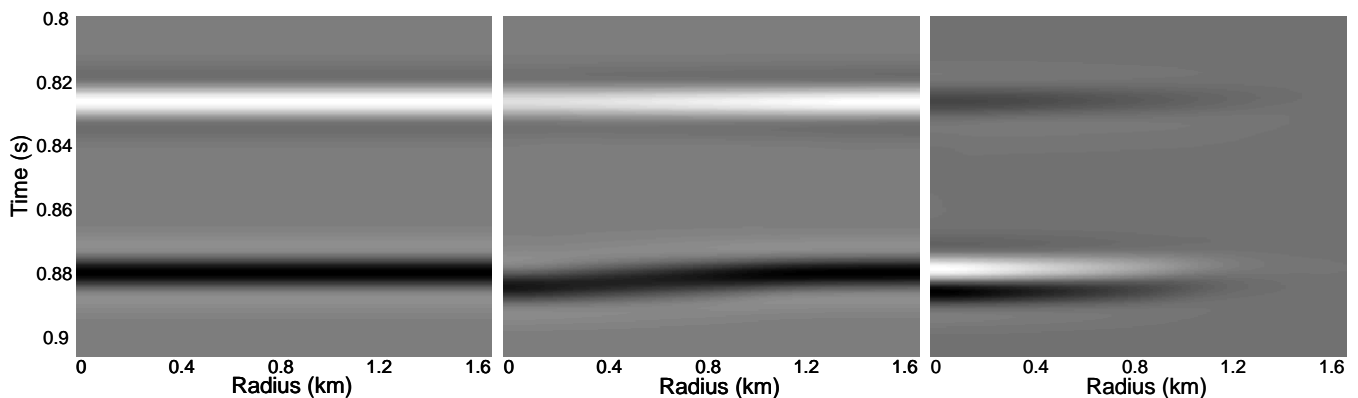


Figure 2.9—(a) Source wavelet and (b) baseline, (c) repeat, and (d) time-lapse synthetic seismic images produced using a convolutional model.

Both pressure and saturation effects will be more noticeable in softer rocks, but nonetheless seismic is still the most viable technique for any setting. Changes in seismic properties are not very dependent on initial pore fluid so there is little difference between its use in aquifers and depleted oil fields. The presence of hydrocarbon gas in the pore space, however, may render seismic monitoring useless. The large initial drop in velocity with increasing CO₂ saturation is a result of the high compressibility of the CO₂ making the effective fluid have more gas-like compressibility. If hydrocarbon gas is also present, the effective fluid already has gas-like compressibility and the addition of CO₂ may not have any noticeable effect.

3. Electromagnetic

While not as popular as seismic methods in the oil industry, electromagnetic (EM) techniques have much to offer in the area of monitoring sequestration. The expected changes in electric and magnetic properties to be measured with electromagnetic techniques, most notably conductivity, may be of an order of magnitude or more, as compared to seismic methods where changes are typically on the order of a few percent. This is not to say, however, that electromagnetic techniques will be more useful than seismic techniques in CO₂ sequestration. Steel casings severely attenuate higher frequency electromagnetic signals, and so reduces the resolution that may be attained. Additionally, common earth materials may vary in conductivity by as much as six orders of magnitude, so detecting an order of magnitude change may prove challenging. Nonetheless, electromagnetic monitoring offers us the ability to measure CO₂ saturations and provides a complimentary set of measurements to seismic.

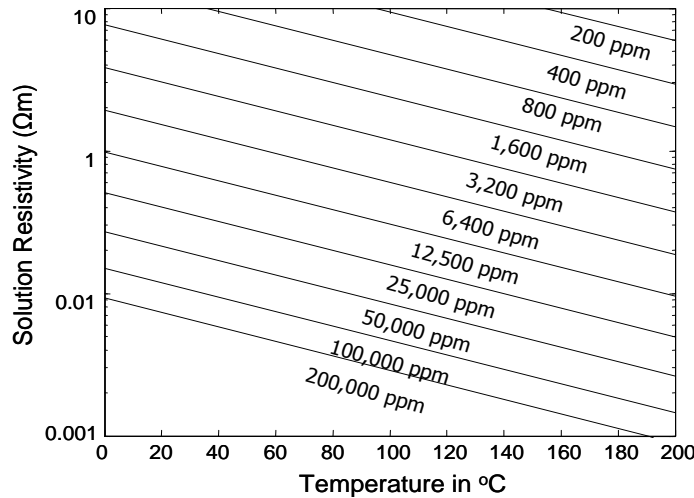


Figure 3.1—Brine resistivity in ohm meters as a function of temperature and salinity.

3.1 Electromagnetic Model

In dealing with field scale electromagnetic measurements, conductivity plays a dominant role in electric and electromagnetic techniques. Rock conductivity is very sensitive to brine saturation and brine conductivity, which is in turn dependent on the salinity and temperature of the brine (Fig. 3.1). CO₂ and other types of initial reservoir fluids are very resistive and have a negligible impact on the bulk conductivity of both the fluid and the rock. Here we will estimate brine resistivity at 18 °C using a polynomial fit (Moore, 1966), then make an approximate temperature conversion (Schlumberger, 1985).

Rock conductivity may be estimated with Archie’s Law and it’s various modifications. It is an empirical formula which must be fit to the reservoir rocks in the area of interest. In it’s basic form, Archie’s law is given by

$$\sigma = \frac{1}{a} \phi^m S_w^n \sigma_w \quad (3.1)$$

This expression relates the bulk conductivity σ of the rock to the porosity ϕ , water saturation S_w , and water conductivity σ_w . a , m , and n are dimensionless constants which will need to be determined for a particular formation, with typical values for clean sandstones around 1, 2, and 2 respectively. Higher values of m have been reported for Middle-Eastern carbonate rocks (Focke, 1987). For shaly sands an additional term is added to the water conductivity to represent the added conductivity of the rock matrix. This modification takes the form

$$\sigma = \frac{1}{a} \phi^m S_w^n (\sigma_w + BQ_v) \quad (3.2)$$

which was first proposed by Waxman (1968). In this expression, B is the average mobility of the ions and Q_v is the charge per unit pore volume. Other work on low porosity carbonates has yielded more complex relationships such as the Shell formula (Schlumberger, 1985)

$$\sigma = \phi^{(1.87 + 0.019 / \phi)} S_w^n \sigma_w \quad (3.3)$$

In general, the constants in the above equations need to be fit as part of site specific characterization. Fig. 3.2 displays conductivity as a function of brine saturation and porosity for a clean sand with the typical values for the Archie's Law constants. The salinity for the brine used in this model is 100,000 ppm, and the temperature is 35 °C. From this model we see that decreasing brine saturation in an aquifer from initially full saturation to 30% saturation results in an order of magnitude change in conductivity, while porosity governs the actual amount of change observed.

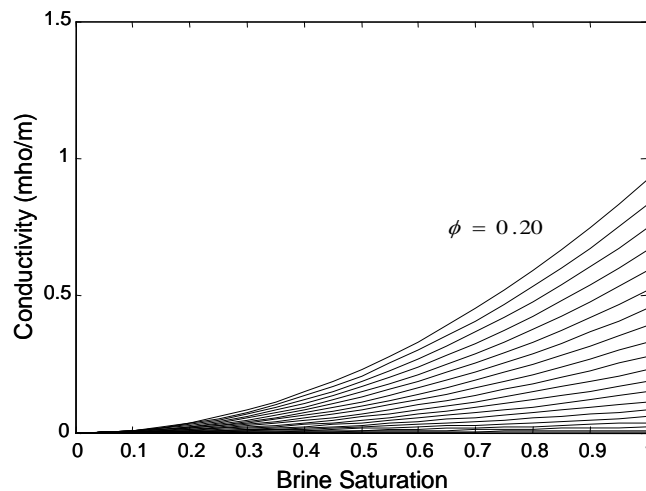


Figure 3.2—Rock conductivity as a function of porosity and brine saturation for a shaly sand with 10% clay content.

Conductivity may be measured directly in the shallow subsurface with electrical resistance

tomography (ERT). In deep reservoirs and aquifers, however, boreholes are widely separated and conductivity measurements need to be made over large distances. Using ERT in this manner produces extremely low resolution images of the subsurface, and so other techniques have been developed for this type of situation. Modern electromagnetic techniques (Wilt, 1995b) make use of magnetic source and receiver dipole antennas to propagate electromagnetic waves over long distances. Early work in this field (Laine, 1987) involved the use of 15 and 17 MHz signals to provide high resolution images using strait ray tomographic techniques. Using such high frequencies, well spacing was limited to several meters.

To propagate the waves several hundred meters kilohertz frequencies need to be used. Using these lower frequencies introduces several complications. The wavenumber for a electromagnetic wave traveling in a conductive medium is complex and is given by

$$k^2 = \mu\epsilon\omega^2 - i\mu\omega\sigma \quad (3.4)$$

Here μ is the magnetic permeability, ϵ is the electric permittivity, σ is the conductivity of the medium, and ω is the frequency in radians per second. In highly conductive materials and at low operating frequency the second term dominates, leading to a diffusive solution to the wave equation. This leads to a “quasi-ellipsoidal” (Spies, 1995) region of high sensitivity between the source and receiver, and strait ray tomographic inversion is no longer appropriate. Nonetheless the received signal is still a nonlinear product of the discrete attenuation contributions of the reservoir rocks and may be inverted for conductivity structure. The attenuation coefficient in this diffusive regime is given by

$$\alpha = \sqrt{\frac{\mu\omega\sigma}{2}} \quad (3.5)$$

A first order approximation of the attenuation using a strait ray approximation can still be useful in predicting the signal strength and attenuation for a given setup. The expect signal for a vertical magnetic dipole transmitters and receivers, assuming exponential variation in time and space, is given by

$$H_z(r, \phi) = \frac{me^{-ikr}}{4\pi r^3} [k^2 r^2 \cos^2 \phi + (3 \sin^2 \phi - 1)(1 - ikr)] \quad (3.6)$$

(Jackson, 1962) where m is the magnetic dipole moment and r is the source receiver separation distance. Substituting in (3.4) and simplifying for the case where the transmitters and receivers are at nearly the same depth with a separation distance several times greater than the skin depth, we get

$$H_z \approx H_0 \frac{e^{-\alpha r}}{r} \quad (3.7)$$

which is essentially identical to seismic attenuation resulting from attenuation and spherical divergence. Here H_0 is the amplitude of the vertical magnetic field one meter from the source. In practice it's been found that operating between about 5 and 10 skin depths provides optimal signal strength and resolution (Wilt, 1995a). It should be noted that this model accounts only for signal reduction due to absorption and does not account for scattering effects.

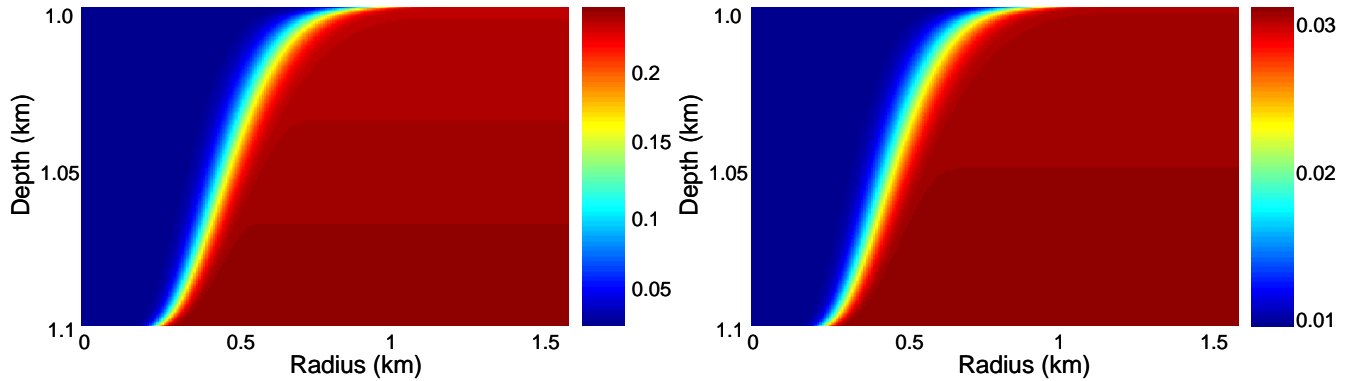


Figure 3.3—(a) Formation conductivity in mho/m and (b) local attenuation in m^{-1} .

3.2 Field Scale Results

Fig. 3.3 shows the electromagnetic results from out injection simulation. As there is no pressure dependence for brine resistivity the conductivity profile simple tracks the saturation profile. We see uniform conductivity in the fully flooded and unflooded regions with approximately an order of magnitude difference which we came to expect from our rock physics model. The local attenuation profile (Fig. 3.3b) changes by a factor of 3 between the flooded and unflooded regions. Like seismic, detailed forward modeling will be required to take conductivity and attenuation profiles such as these and convert them to measured signals. Strait ray methods are not appropriate for low frequency measurements and only provide a first approximation of the expected attenuation.

Resistivity surveys like ERT are the simplest method of assessing subsurface conductivity. At the large separation distances required for monitoring CO_2 sequestration such techniques will detect only the average changes in the reservoir and may be of too low resolution to be of any use. The other option we've discussed is crosswell electromagnetic measurements. At the low frequencies necessary to propagate EM waves field scale distances the measurements the resolution is fairly low and the measurements are strongly affected by the conductivity structure near the source and receiver. Carrying out a crosswell EM survey is cheaper and easier than it is for a crosswell seismic survey; coupling is not an issue and the boreholes may be dry or wet.

Perhaps the most important consideration in the use of electromagnetic monitoring is the effect

of well casing. Steel cased wells attenuate electromagnetic signals above about 10 Hz and severely attenuate signals in the hundred hertz range and higher. While this has traditionally been a problem for electromagnetic monitoring, recent studies have found that the response of the casing is fairly easy to model and that the effect may be removed from the total measured field without great difficulty (Wilt, 1998). Another option available is the use of fiberglass monitoring wells to carryout EM surveys, or to place insulating gaps in the casing and use it itself as a pair of electrodes (Nekut, 1995).

Electromagnetic techniques are not strongly dependent on rock type, rock strength, or formation depth, but are dependent on initial and final fluid saturations. Aquifers will be the best candidates for electromagnetic monitoring as they will have the largest brine saturation changes and therefore the largest conductivity and attenuation change. Changes in R_{CO_2} over time are not expected to greatly change the conductivity of the formation fluid, though there will be some additional conductivity associated with the additional ions in the fluid from the formation of carbonic acid.

4. Gravity

The last two techniques we'll discuss are gravitational and geodetic techniques which are very similar from a modeling standpoint. The model we'll be using is Newtonian gravity. Changes in pore size from increased pore pressure are expected to be negligible compared to the change in gravity resulting from fluid density changes (Eq. 2.3). Gravity is a low-resolution technique with fundamentally non-unique solutions. Constraining inversions with formation geometry and using only time-lapse information can result in much better results.

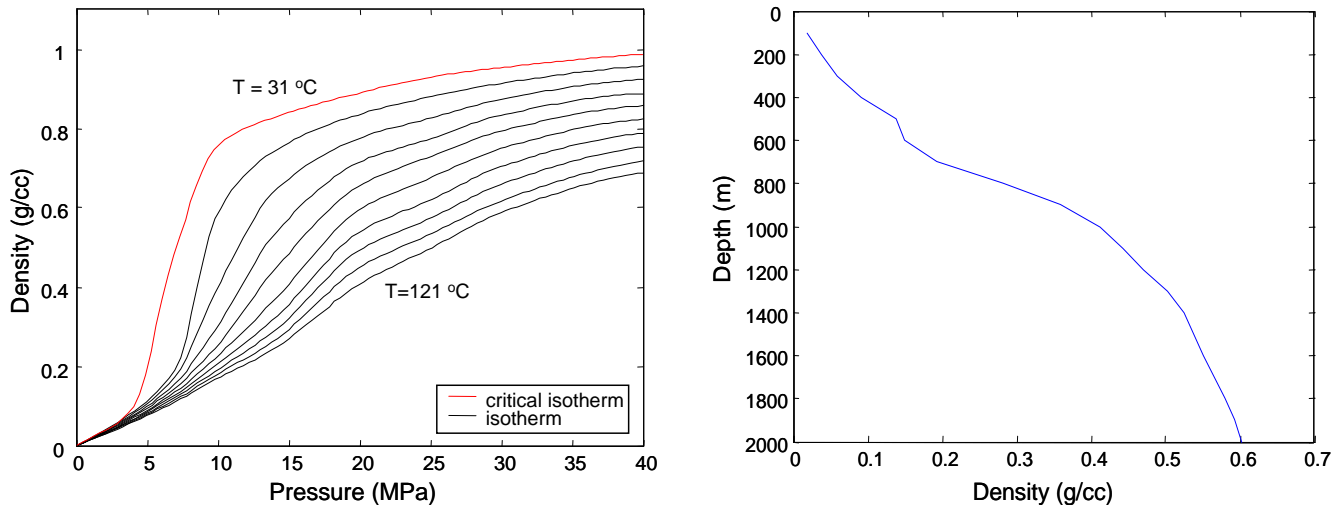


Figure 4.1—(a) CO₂ density as a function of pressure and temperature and (b) as a function of depth with a hydrostatic pressure gradient and a typical geothermal gradient.

4.1 Gravity Model

Brine and oil density are relatively insensitive to changes in pressure and even to increased CO₂ in solution. Almost all of the changes in fluid density associated with CO₂ injection will be from the lower density of the CO₂. Fig. 4.1 shows the density of CO₂ as a function of depth with a hydrostatic pressure gradient and a typical geothermal gradient (a), and also and as a function of pressure and temperature (b). It is apparent that as the formation depth increases the CO₂ density will increase to the point where there is very little density contrast between the CO₂ and the initial reservoir fluid, in which case there will be no measurable anomaly.

Newton developed his law of gravitation in the 17th century, which today we know to be strictly true at non-relativistic speeds. Unlike many relationships in geophysics, is not approximate or empirical. The perturbation to the gravitational field due to a point source with some discrete volume dV , porosity ϕ , and density change $\Delta\rho$, at a distance r is given by

$$\Delta \bar{g}(r) = -\phi \Delta \rho_{\beta} G \frac{\hat{r}}{r^2} dV \quad (4.1)$$

In general the reservoir will have a complex geometry and variable saturation due to formation heterogeneity, and as such the contributions of discrete points of density change will need to be summed to find the change in the gravitational field. This solution has the form

$$\Delta g_i(\bar{x}) = -G \int dV_{\xi} \phi \Delta \rho_{\beta} \frac{x_i - \xi_i}{|\bar{x} - \bar{\xi}|^3} \quad (4.2)$$

where Δg is the change in the gravitational field at position x and ξ is the spatial variable for the distribution of density changes. This expression is very similar to the deformation model (Eq. 5.2) which will be discussed in the next chapter. Clearly, a stronger signal will result from shallower reservoirs and higher density contrasts. Porosity will have less of an effect as reducing the porosity will simply force the CO_2 to occupy the same pore volume, but in a larger bulk volume.

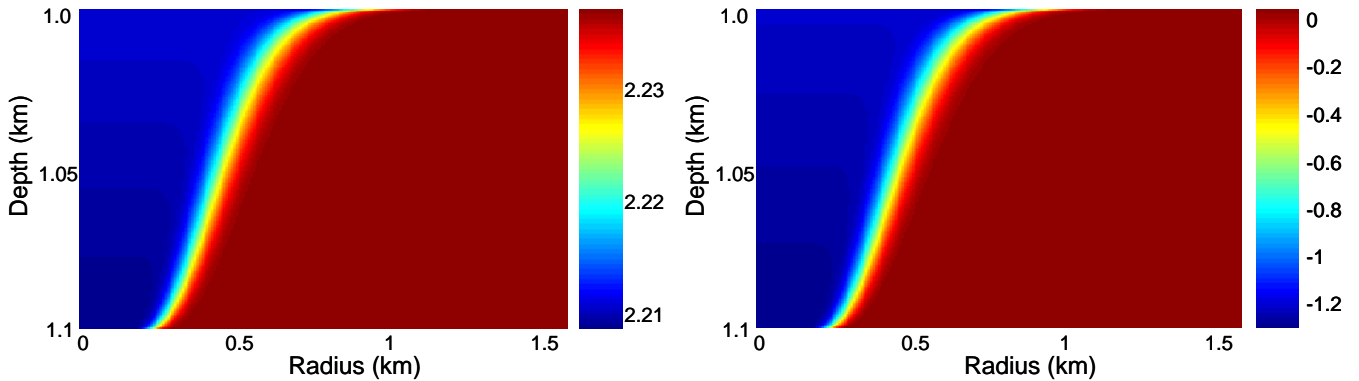


Figure 4.2—(a) Bulk density and (b) bulk density percent change. The background density in our model (dark blue) is 2.25 g/cc.

4.2 Field Scale Results

We can see that the bulk density percent changes are small (Fig. 4.2) which is expected as the CO_2 density is about 0.6 g/cc and the bulk of the mass is in the rock matrix. The gravity change for our homogenous formation is shown in Fig. 4.3. The curves are for profiles at constant depth, and the radius is measured from the center of the injection well. For example, the measured time lapse gravity signal after 10 years of injection directly over the injection well at a depth of 600 meters would be approximately 30 microgals, well above instrument sensitivity in the in the absence of cultural noise.

All of the methods available to measure gravity focus on the gravimeter. These are typically used for surface surveys and have around 10 microgal resolution; newer gravimeters may have resolution as low as one microgal. Collecting a typical surface survey is inexpensive compared to the other techniques we've examined. Downhole data can also be collected in monitoring wells, and higher

resolution microgravity measurements may provide more information on CO₂ movement in the subsurface. Of the monitoring goals we're interested in, gravity is most suitable for making mass balance measurements. Such measurements do not require high resolution (which gravity does not have) and depended only on bulk measurements. Gravity may also be of use in monitoring CO₂ dissolution, as well as in detecting leakage plumes into overlying aquifers.

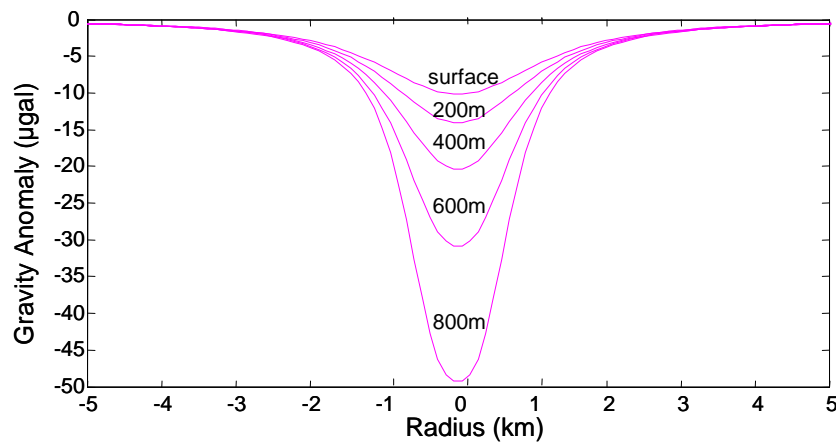


Figure 4.3—Time lapse gravity change as a function of depth and radius from the injection well center. Profiles are at constant depth.

Gravity changes are fairly independent of initial fluid saturations and rock types. Temperature and pressure govern the density contrast, but in general shallower reservoirs will lead to lower CO₂ densities and higher contrasts. Shallow formations are also favorable as the signal falls off inversely with distance squared. From these two effects it is evident that gravitational techniques may only be of any real use either for monitoring shallow reservoirs or for making point measurements in monitoring wells.

5. Deformation

Geodetic techniques measure displacements or displacement gradients at the earth's surface. Such techniques are commonly used in the study of earthquakes or volcanoes, but they may also have applications in monitoring CO₂ sequestration under certain conditions. In a stable tectonic environment, measured deformation over a sequestration site should only be the result of induced pressure changes at depth due to fluid injection. The magnitude of deformation resulting from a point source, also called a “nucleus of strain”, is known. Integrating this point solution over the region of pressure change will produce an arbitrarily complex surface deformation model. Such techniques have been used to explain land subsidence associated with oil production (Geertsma, 1973).

5.1 Deformation Model

In a mechanical sense, fluids only contribute to surface deformation through the pore pressure changes that they carry. That said, the more compressible the reservoir fluids and the larger the volume of reservoir fluid, the less pressure buildup will occur. Boundary conditions also have a large impact on the pressure increase. Open boundaries, such as might be found in an aquifer, will prevent any permanent pressure change as any perturbation to the hydrostatic pressure will eventually diffuse away. The greatest pressure buildup, and consequently the greatest deformation signal, will likely occur in closed oil fields. The viscous oil will cause pressure buildup around the well, and the closed boundaries will lead to an overall increase in formation pressure as more fluid is injected into the system. The attributes which make a formation favorable for geodetic monitoring are, however, not desirable for CO₂ storage. Increasing formation pressure can jeopardize the integrity of the cap rock by inducing faulting.

The deformation model we use is tied into the theory of poroelasticity. While elasticity is the linear theory governing the relationship between stresses and strains in the earth or any rigid body, the governing theory over the elastic behavior of a porous rock is poroelasticity. For highly compacted rocks, with little or no pore space, elasticity is sufficient to explain observed behavior, but in the areas of interest to the petroleum industry or in CO₂ sequestration poroelasticity must be considered. The fundamental relation for poroelasticity (Biot, 1941) relating stress ϵ , to strain σ , and pore pressure p is given by:

$$2\mu\epsilon_{ij} = \sigma_{ij} - \frac{\nu}{1+\nu}\sigma_{kk}\delta_{ij} + \frac{1-2\nu}{1+\nu}\alpha p\delta_{ij} \quad (5.1)$$

In this notation the strain, ϵ , is positive for extension from a reference equilibrium state, p is the pressure change from a reference pore pressure, and the stress σ is positive for increased deviatoric tensional

stress. Other constants in this expression are the Biot coefficient α , Poisson's ratio ν , and the shear modulus μ . δ is the Dirac delta function.

To calculate deformation we integrate over the Green's Function solution (Appendix A) for a point pressure source in a halfspace (Segall, 1992; Vasco, 1998). An alternate solution is to couple poroelastic theory with the so-called Mogi model (Mogi, 1958). The solutions for both are identical and are given by

$$u_i(\bar{x}) = \frac{1}{2\pi} \int_V dV_\xi \frac{1-2\nu}{\mu} \alpha p(\xi) \frac{x_i - \xi_i}{|\bar{x} - \xi|^3} \quad (5.2)$$

where u is the displacement vector at point of measurement x on the free surface ($x_3 = 0$) and ξ is the spatial variable for the distribution of pressure change. Important to note is that the magnitude of deformation is linearly related to pressure change, inversely related to the rock modulus, and falls off inversely with distance squared.

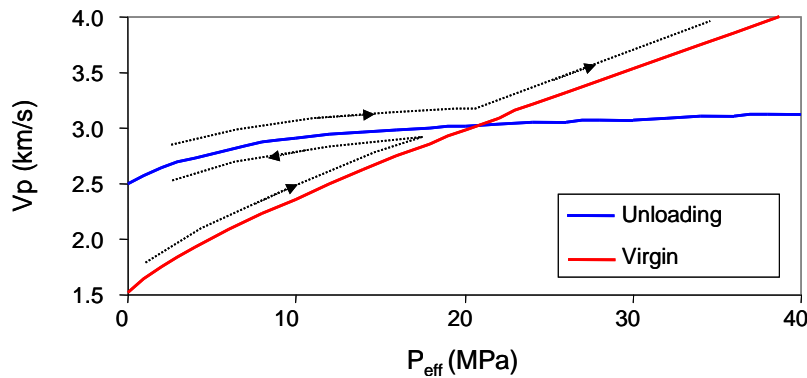


Figure 5.1—Bowers' virgin curve and Eberhart-Phillips unloading curve behavior.

An important difference between surface subsidence seen in producing oil fields and uplift expected from sequestration lies in the magnitude of expected deformation. While the fundamental equations are unchanged between the two cases, the effective modulus may be very different. This occurs mostly in poorly consolidated sandstones as increasing effective stress, by decreasing the pore pressure with a constant overburden, results in the compaction of the rock along the “virgin curve” (Bowers, 1994), a process which changes the moduli of the rock. Decreasing the effective stress, however, causes the rock to unload on a different curve described by Eberhart-Phillips (Fig. 5.1), which is nearly elastic for small pressure perturbations.

A rule of thumb is that the ratio of the compaction coefficient to rock compressibility is approximately ten to one, meaning that ten times as much subsidence is expected to be associated with a

negative pore pressure change as would occur from a positive pressure change of the same magnitude. For subsidence, depending on the type of reservoir rocks present, either elastic compression or inelastic compaction may occur. Elastic compression normally occurs in very hard rocks like carbonates or upon reloading of sandstones.

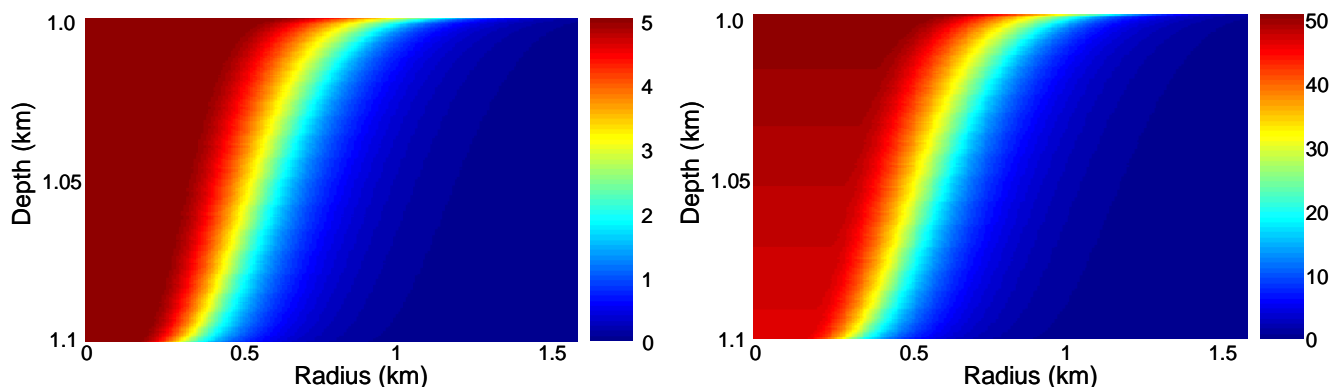


Figure 5.2—Pore Pressure change in MPa from initial pore pressure.

5.2 Field Scale Results

Fig. 5.3 shows the deformation and tilt results associated with the pressure changes given by our model (Fig. 5.2). One millimeter of displacement is well below the detectability threshold of modern instruments; instrument sensitivity is typically on the order of one centimeter of vertical resolution for continuous GPS and InSAR (interferometric synthetic aperture radar). GPS has the better sensitivity while InSAR is desirable because of the low cost of processing and the wide spatial coverage. Given this sensitivity, depending on the depth, rock type, and pressure changes detecting signals from sequestration may not be possible using either of these techniques. A more useful techniques may be the use of tiltmeters as the one microradian predicted by our modeling represents a very detectable signal. Tiltmeters may have sensitivities as low as 0.1 microradian, below the peak expected signal from only one year of injection in our model.

Surface geodetic techniques, much like gravity, are low resolution techniques. Source geometry is poorly constrained for inversion and as such it is likely that in any sequestration monitoring application would be focused more on mass balance and bulk storage of on CO₂ than on CO₂ migration and leak detection. Downhole tiltmeters have been suggested for measuring deformation at a more local level. Such instruments could potentially detect deformation associated with hydrofracs in low porosity carbonates (Wawersik, 2001), as well as providing more focused data on pore pressure changes.

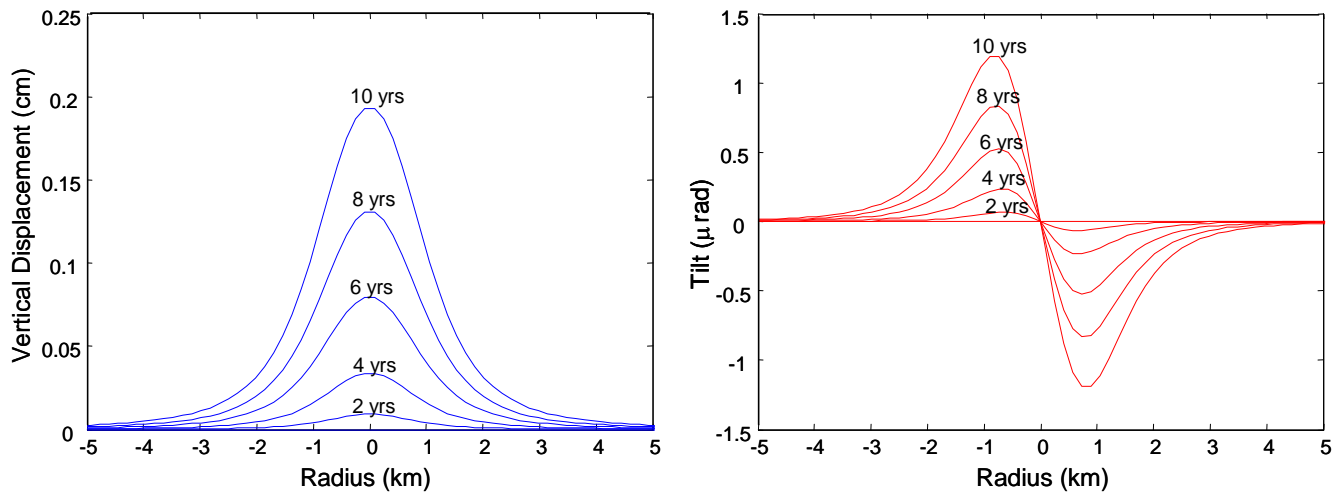


Figure 5.3—Deformation results after 10 years of injection. (a) Vertical surface displacement and (b) surface tilt for a surface profile passing over the injection well.

As the signal is strongly dependent on the depth, rock type, and pressure buildup, sites will need to be assessed on a case by case basis for usefulness of these geodetic techniques. In general, smaller systems with closed boundaries, as are commonly found in oil reservoirs, will lead to larger pressure changes and greater signals. Large open systems, like brine aquifers, may have virtually no pressure changes if permeability is sufficiently high. The presence of a large gas cap would also have a significant effect on pressure changes. Having a large volume of highly compressible gas would reduce any pressure increase resulting from injection.

6. Sleipner Seismic

The Sleipner field is offshore Norway in the North Sea and is considered to be the first pure sequestration project in the world. The Saline Aquifer CO₂ Storage project (SACS), who is responsible for monitoring the injection, has almost exclusively used seismic monitoring and have produced high quality time-lapse images which highlight changes associated with the presence of CO₂. Our study will illustrate the usefulness of coupling our geophysical models with flow models. Flow models provide a useful tool for determining optimum technology in monitoring a given formation undergoing CO₂ injection. Flow models also stand to benefit from the integration of geophysical monitoring in areas of verification and refinement of the flow model (SACS, 2003). In the interest of confirming the modeling discussed above we will compare our seismic modeling results with the time-lapse seismic images from Sleipner.

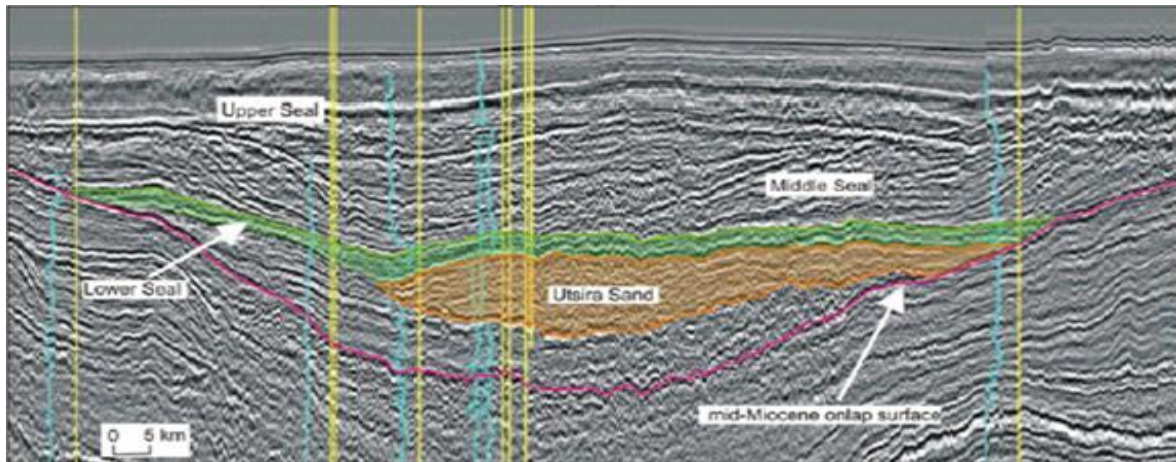


Figure 6.1—Reflection image of the Utsira sand (SACS).

6.1 Geologic Setting

The Utsira formation is an elongated sand aquifer approximately 1000 meters in depth. The formation is several hundred meters thick, with an area close to 25,000 km². At Sleipner CO₂ is produced with petroleum gas from the Sleipner east field, separated, and reinjected into a shallower aquifer, the Utsira Sand (Fig. 6.1). Injection began in 1996 and to date more than 5 MMt of CO₂ have been injected in the field, currently at a rate of approximately 1 MMt/yr (Torp, 2002). CO₂ is injected from a horizontal well at the base of the formation, from which it is driven upward by buoyancy effects. Injection depth is approximately a kilometer beneath the sea floor thus the CO₂ is in a supercritical state. The primary trapping mechanism in the short-term will be hydrodynamic trapping, followed by long-term solubility trapping as the CO₂ is dissolved in the formation brine.

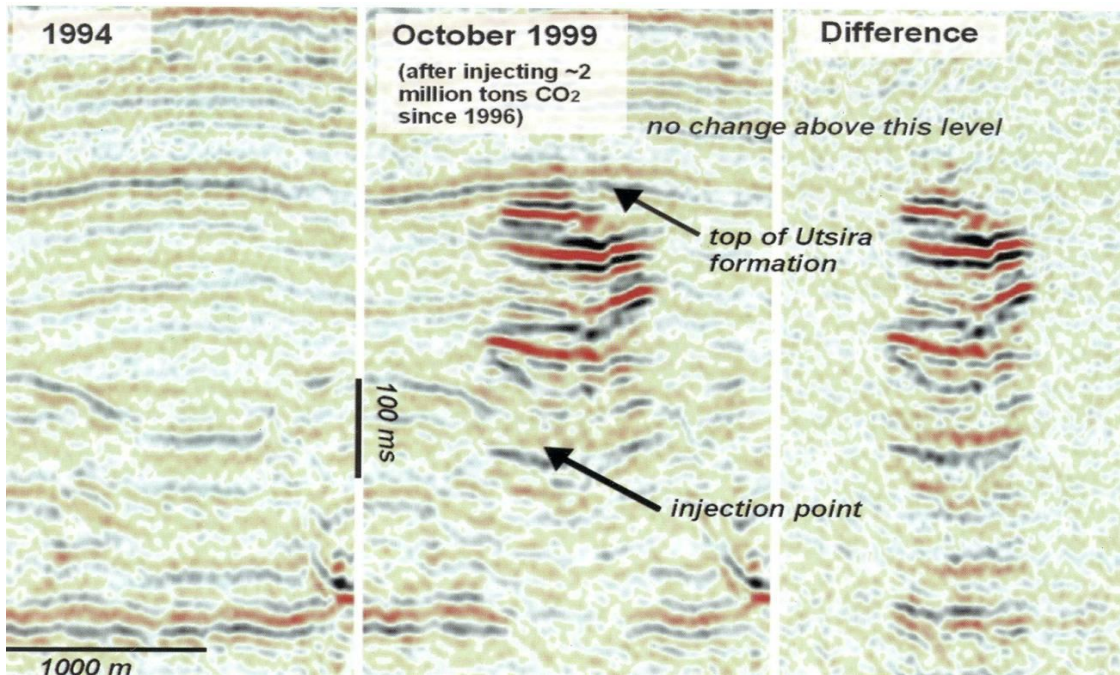


Figure 6.2—Time-lapse seismic image (SACS).

Sleipner is unsuitable for many of the monitoring techniques discussed in this report. Due to the high permeability, huge lateral extent, and small gas column heights there is no expected or observed pressure accumulation, ruling out the use of geodetic techniques or passive seismic monitoring. Seismic has proven to be effective, while gravity has not been used, nor have electromagnetic methods. Through seismic interpretation thin, previously undetectable shale layers have been illuminated through the use of time-lapse seismic imaging, and CO₂ layers as thin as one meter have been identified. This sensitivity has given them confidence that any leakage into the overlying formations would be easily detectable, and, as no seismic changes in the overburden have been detected, that the CO₂ is being contained (Arts, 2002).

6.2 Sleipner Model

The model of Sleipner (Fig. 6.3) used here was created using Eclipse 300. The injected CO₂ rises, by molecular diffusion and Darcy flow, through thin permeable shale layers. The model consists of three years of injection followed by 100 years of migration and dissolution. As the injected CO₂ rises through the aquifer it spreads out and pools beneath the shale layers, dissolving in the formation brine over time. The geometry shown is half of a cross-section with the injection point, representing an infinite horizontal pipe, at zero radius and 160 meters below the reservoir seal. The thickness of the tabular reservoir is 180 meters and the maximum horizontal distance is 6 km.

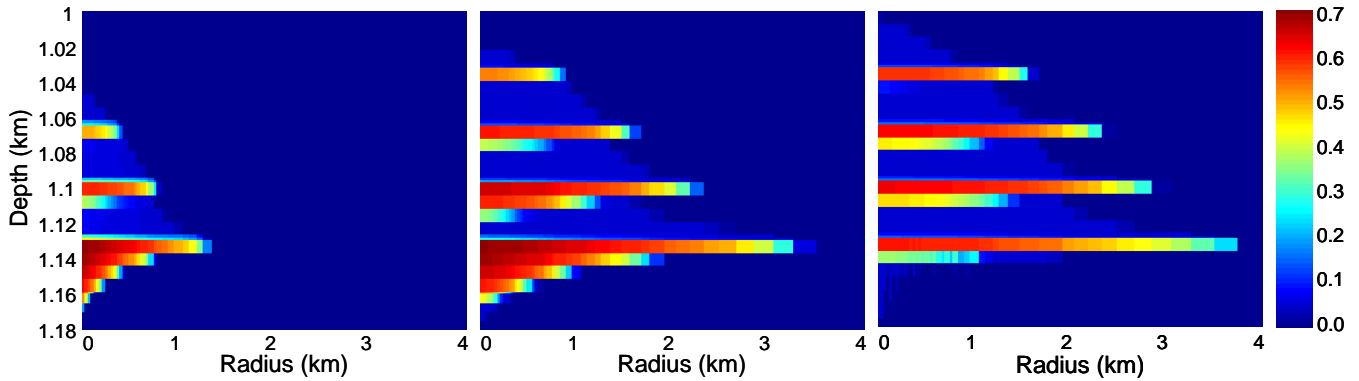


Figure 6.3—Saturation images for a simplified Sleipner injection model with thin shale layers as a function of depth and horizontal distance from the injector at 1, 5, and 20 years.

Just as we did with the seismic model previously, we can use pressure and saturation cross-sections and some knowledge of the formation rocks to produce density, velocity, and impedance maps. From these maps we are able to produce synthetic seismic and time-lapse seismic images using the same convolutional model used above. The model has high permeability which lead to negligible pressure changes. As such the pressure is simply hydrostatic in the formation, and all of the interesting changes are a result of saturation changes.

6.3 Field Scale Results

The synthetic and time-lapse seismic images clearly show the effects of the CO₂ bubble. In the synthetic reflection images (Fig. 6.4) one can see the effect known as reflector pull-down resulting from the slower velocities in the CO₂ saturated regions. The effect is cumulative so the later arrivals display a greater pull-down than the early arrivals. It is somewhat difficult to tell from these plots, but the amplitude of the shale reflections, with CO₂ pooled underneath, are greater than in the areas with no CO₂. These bright spots are a result of a difference in the impedance contrast between the top of the shale and the bottom, and are indicative of the presence of CO₂. At large distances from the well there is no CO₂ saturation and the reflections are simply the reflections off of the thin shale layers. The time-lapse images (Fig. 6.5) very clearly display the CO₂ saturated region and, in a more complex geology than the simple layered model we use, would be more useful than the reflection image for determining the location of CO₂.

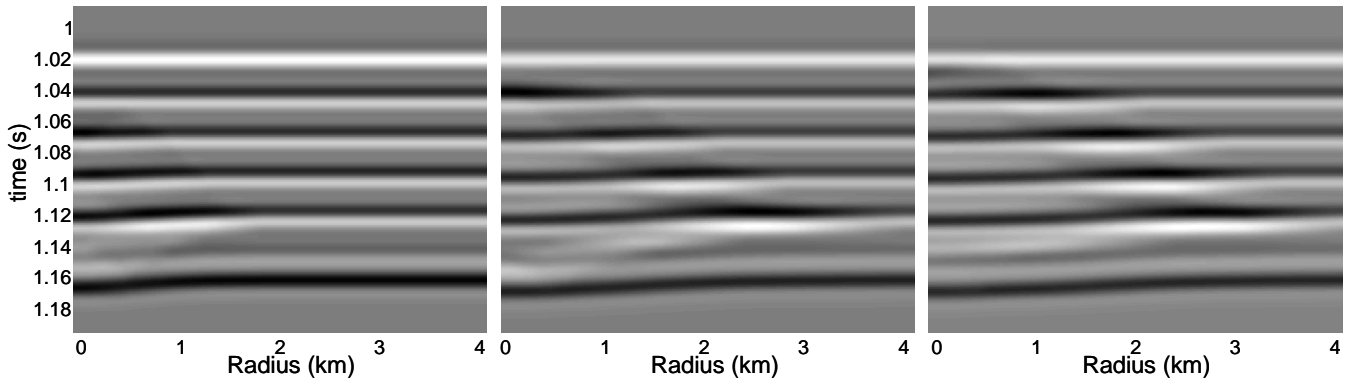


Figure 6.4—Synthetic seismic images as a function of time and horizontal distance from the injector.

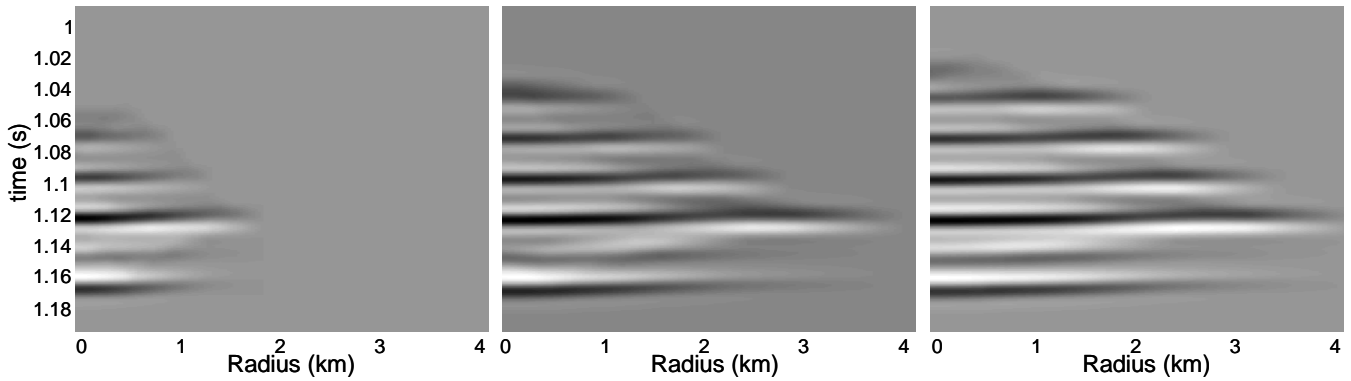


Figure 6.5—Time-lapse seismic images as a function of time and horizontal distance from the injector.

Both of the pull-down and the bright spot effects are seen in the Sleipner seismic and time-lapse seismic images (Fig. 6.2), qualitatively verifying our seismic modeling. For a more complicated reservoir model based on a real reservoir it would be necessary to do more complex forward modeling such as ray tracing or wave-field modeling.

7. Elk Hills Deformation

To illustrate the utility of geodetic techniques for measuring deformation associated with sequestration, we examined deformation over Elk Hills between Nov. '92 to Nov. '95 using InSAR. We did not chose a sequestration site or natural analog site for this test for several reasons. First, that the magnitude of deformation is expected to be greater for subsidence than for uplift. Second, that the existing sequestration sites with enough history to enable the use of InSAR are underwater (in the case of Sleipner) or in an area with little coverage (in the case of Weyburn). Third, that most of the natural analog sites are in areas with steep and rapidly varying topography (the Rocky Mountains). Elk Hills was desirable because of its history of InSAR coverage to draw from, its arid climate, and its large production rate.

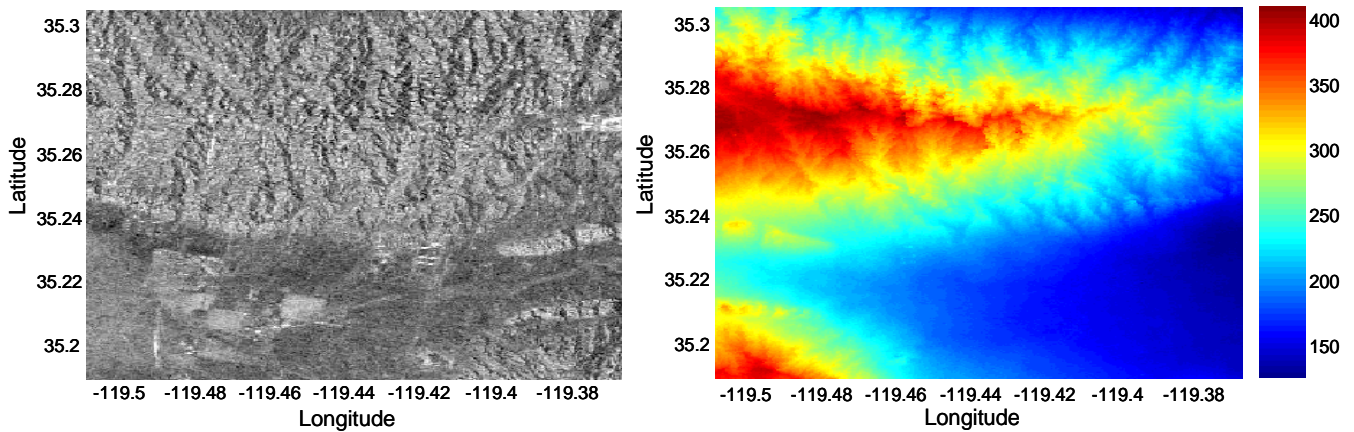


Figure 7.1—InSAR (a) amplitude image and (b) elevation map in meters over Elk Hills.

7.1 Geologic Setting

Elk Hills is a large producing oil and gas field located approximately 40 km southwest of Bakersfield, California, in the southwestern part of the San Joaquin basin. Fig. 7.1a shows an amplitude reflectivity image of the region of interest. Oil was discovered in Elk Hills in 1919. The field remained mostly inactive as a naval strategic petroleum reserve until 1976 at which time production was started in earnest. The field continued to be operated by the government until February 1998 when Elk Hills was sold to Oxy. The period we are interested in is the early 1990's while the field was still under government control.

The reservoir can be broadly divided into the Pliocene shallow oil zone (SOZ) and the deeper Miocene Stevens formation. The SOZ consists of numerous sand and shale layers with nearly vertical NW-SW striking normal faults running throughout. The reservoir rocks are predominantly unconsolidated sandstones with depths of 600 to 1400 meters subsurface. About half of the fields

production is from the SOZ. The Eastern Shallow Oil Zone (ESOZ) has undergone constant gas injection since production was begun and through the period in question. The deeper Sevens formation is a series of anticlines which form traps for large sandstone oil pools. The sandstone is of turbidite origin and lies between 1500 to 3000 meters depth. Both waterflooding and gas injection have been used continuously as a secondary recovery technique. The oil produced in the Stevens has an average API of about 35 deg (Maher, 1975).

During the period of interest the Elk Hills field produced about 60,000 barrels of oil per day and about 400 mcf/d of natural gas. There are over 1000 producing wells, with approximately half targeting shallow zone and half targeting the deeper horizons. The productive area is approximately 115 km² along the crest of the hills and the variation in topography over the area of interest is about 300 meters (Fig. 7.1b). The productive area of the SOZ is over 80 km².

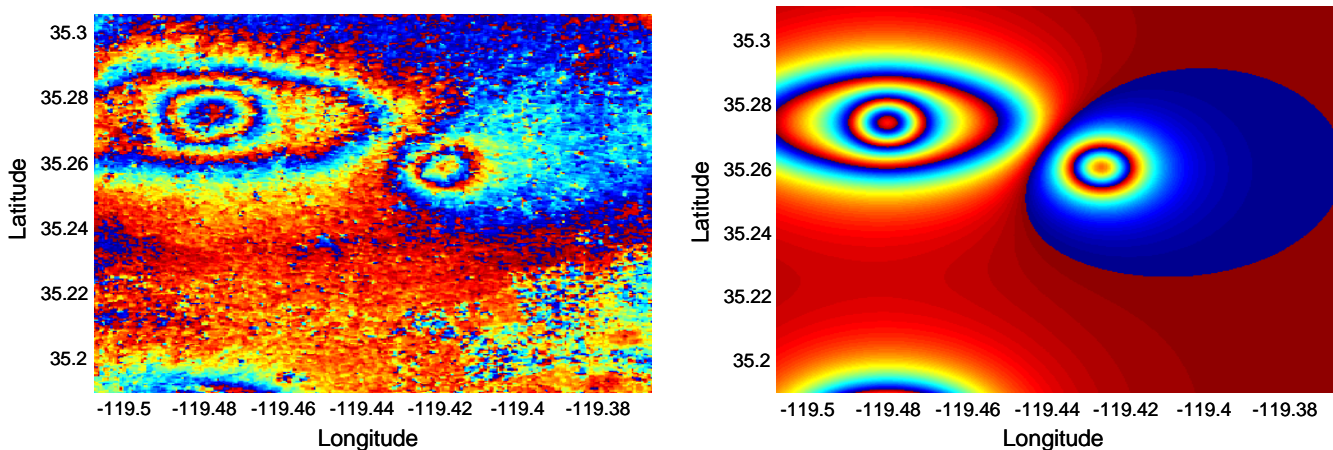


Figure 7.2—InSAR (a) collected data and (b) deformation model over Elk Hills.

7.2 Elk Hills Model

The InSAR deformation images produced over Elk Hills showed areas of both subsidence and uplift. The two types of areas received separate but similar treatment as discussed previously, compaction for the subsidence and approximately elastic expansion for the uplift. Production at Elk Hills lowered the pore pressure, thereby increasing the effective stress. As the reservoirs we are examining here consist primarily of sandstone which has been produced continuously for over twenty years, it is clear that the observed subsidence over Elk Hills is due to compaction.

The area of subsidence occurs exactly over the 31S reservoir in the deeper Stevens, which can account for the broad subsidence seen in Fig. 7.3a. The area of inflation and the rapidly varying subsidence in the center of the area of subsidence (Fig. 7.2a) must be a result of shallow processes. It's probable that the high subsidence signal seen in the center of the larger signal is a result of local pressure

changes in the ESOZ, and that the inflation pattern observed is caused by shallow pressure changes associated with water disposal. As mentioned in the deformation discussion above it is much more difficult to achieve large amounts of uplift, compared to subsidence, meaning that the uplift seen in the data, if accurate, must be due to larger pressure changes or much shallower depths than the subsidence signal. To model the pattern observed in the InSAR data we use pressure sources in the shape of thin elliptical disks for the larger, deeper sources, and thin circular disks to model the shallow behavior.

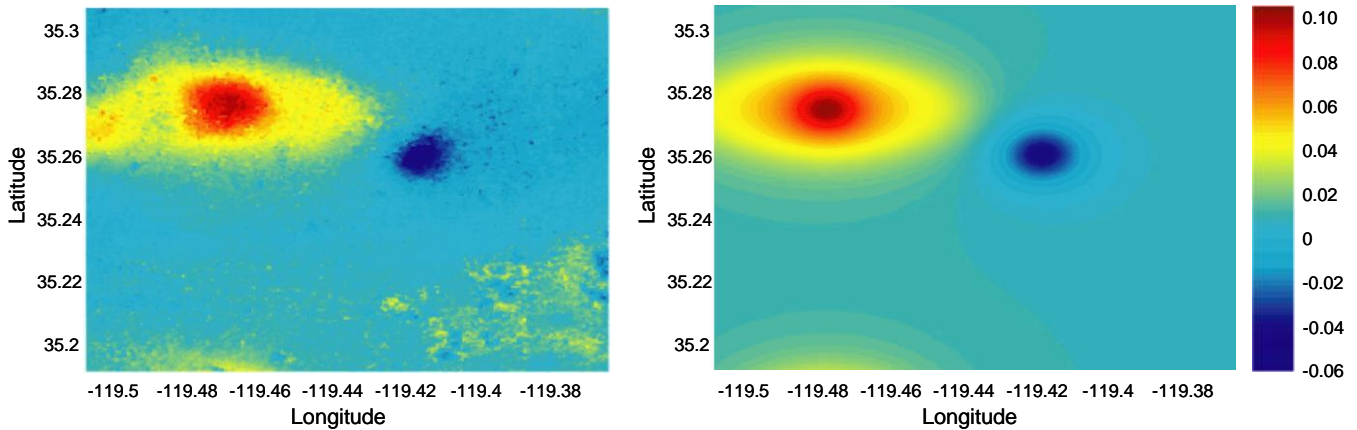


Figure 7.3—(a) Deformation signal and (b) deformation model over Elk Hills in meters.

7.3 Field Scale Results

Figure 7.2a is the InSAR interferogram that we produced spanning this three year period. The large fringe pattern corresponds to the crest of Elk Hills, the primary production zone, directly over the Stevens anticline. The peak magnitude of the subsidence observed is approximately 10 cm, well above the resolution limit of the instruments under good atmospheric conditions. Detecting this magnitude of inflation over this time period was an unexpected result, though the amount of water being disposed of in the subsurface is sufficient, under the proper conditions, to cause the observed uplift.

Using the point source deformation model (Eq. 5.2) we were able to successfully model the observed subsidence pattern with reasonable pressure changes in elliptical disks of reasonable size corresponding to the SOZ and the Stevens reservoirs. Examining Figs. 7.2 and 7.3 show clear quantitative and qualitative correspondence to the collected data. This result does not, however, testify to the usefulness of InSAR for monitoring CO₂ injection. Even if similar magnitudes of pressure changes were to occur in an identical reservoir undergoing CO₂ injection there would be approximately one tenth of the observed signal. This is due to the difference between compaction coefficients and elastic compressibility discussed previously. In that case the signal would be approximately equal to the sensitivity of the instrument under typical atmospheric conditions and one would have a much more challenging task to identify and interpret that signal.

8. Conclusions

8.1 Summary of Results

While it would be very difficult to accurately predict the values of the physical parameters in a real formation either before or after CO₂ injection, accurately predicting time-lapse changes from a baseline survey is much easier. Most of the geophysical models used here are either empirical relations or are true for an idealized isotropic elastic material. Using models such as these provide only approximate solutions but give valuable insight into the behavior of these systems.

The results of the above discussions are summarized in Table 8.1. Not surprisingly seismic, being the highest resolution technique, has the widest range of uses and is not limited by geologic setting except as previously noted. The SACS project at Sleipner has certainly confirmed the ability of seismic monitoring to track CO₂ in the subsurface. High resolution 3-D seismic is also one of the most expensive techniques to use, costing on the order of a million dollars per survey. While this cost is high, when compared to the expected costs sequestration it should not constitute a very significant expense (Meyer, 2002).

These monitoring techniques also need not be used independently. LBNL conducted a study at the Lost Hills field in southern California during a CO₂ injection pilot study (Hoversten, 2002). They used both high resolution crosswell seismic and electromagnetic monitoring to find compressional and shear velocities as well as conductivity. Using the combination of these methods they were able to separate pressure and saturation changes from R_{CO₂} effects. Using combination of techniques to constrain our models may prove necessary to reach our monitor goals for CO₂ sequestration.

	Seismic	Electromagnetic	Gravity	Deformation
Mass Balance	low res.	low res.	good	good
CO₂ Migration	good	good	low res.	low res.
Leak Detection	good	good	low res.	no
Geologic Setting	any (no gas)	aquifers	any	oil and gas
Rock Strength	any (soft better)	any	any	soft
Formation Depth	any	any	shallow	shallow

Table 8.1—Summary of the usefulness of geophysical techniques by use and setting.

8.2 Future Work

One of the most important steps in continuing this research would be to participate in a field study. Such a study would need to involve site specific characterization for calibration of our rock physics models, coupling with flow models to predict the performance of geophysical methods, and detailed seismic and electromagnetic forward modeling to predict time-lapse changes. Comparing these results with the inversions of real measurements made as part of the study would yield valuable insight into the usefulness of geophysical modeling.

Another productive area of research would be to develop a monitoring timeline for the cost effective and effective monitoring of a given site over its lifetime. When planning to monitor a reservoir for ten to perhaps hundreds of years it no longer remains a simple question of detectability. The monitoring techniques discussed above have survey costs ranging from hundreds of dollars to acquire InSAR data, to millions of dollars for high resolution seismic. This approach would not try to choose the absolute best technique, but rather make use of a suite of techniques over the lifetime of a sequestration site to carry out the necessary monitoring. An example of this approach for the monitoring of a shallow aquifer might be to use high resolution seismic to monitor the initial injection period, followed by microgravity to monitor the containment and dissolution of the waste CO₂. This sort of timeline will be site specific, as are the monitoring options discussed in this research.

Including R_{CO_2} in our models should be very straightforward. As mentioned in the introduction the dissolution is expected to occur on a longer timescale than injection, but as monitoring will not be limited to the injection period this effect will need to be accounted for in any long term modeling. Changes associated with R_{CO_2} will still, in the long-term, be secondary compared to changes associated with saturation changes. However, if we hope to be able to track CO₂ in solution then modeling these effects will be necessary.

Appendix A: Green's Function Derivation

Once the pressure distribution at depth is determined, the resulting surface deformation may be modeled. To achieve this we use the approximation of an isotropic, homogeneous poroelastic half-space. While certainly not an accurate description of the real subsurface, this approximation is capable of providing meaningful results (Mogi, 1958; Vasco, 1988).

Two equivalent methods of solving this deformation problem are either by seeking a Green's Function solution for the displacement potential or by integrating a point Mogi source. To find the Green's Function solution we introduce a displacement potential for a full space, Φ , such that

$$\nabla^2 \Phi = \left(\frac{1-2\nu}{1-\nu} \right) \frac{\alpha p(x)}{2\mu} \quad \text{and} \quad \frac{\partial \Phi}{\partial x_i} = u_i \quad (\text{A.1})$$

(Segall, 1992). In these expressions μ and ν are respectively the shear modulus and Poisson's ratio of the halfspace, p is the pore pressure change and is a function of position, u is the component of displacement, and α is the Biot coefficient. Seeking a Green's Function solution to the potential for an arbitrary pressure distribution results in the solution

$$\Phi(\bar{x}) = \int G(\bar{x}, \bar{\xi}) \left(\frac{1-2\nu}{1-\nu} \right) \frac{\alpha p(\bar{\xi})}{2\mu} dV_{\bar{\xi}} \quad (\text{A.2})$$

dV is the differential volume element in which a pressure change p occurs, $\bar{\xi}$ is the spatial variable for the location of the pressure changes, x denotes the measurement position, and G is the Green's Function solution to the Laplacian given by

$$G(\bar{x}, \bar{\xi}) = - \frac{1}{4\pi |\bar{x} - \bar{\xi}|} \quad (\text{A.3})$$

The displacements for a half-space may then be found using the potential field of the pressure source and an image source using

$$\bar{u} = \nabla \Phi + \nabla_2 \Phi_2 \quad (\text{A.4})$$

(Mindlin, 1950), where Φ_2 is an image potential reflected across the free surface and the second gradient term is defined by

$$\nabla_2 = (3-4\nu)\nabla + 2\nabla_z \frac{\partial}{\partial z} - 4(1-\nu)\hat{e}_z \nabla^2 z \quad (\text{A.5})$$

This term is introduced to remove the tractions on the $x_3 = 0$ surface. Evaluating the resultant displacements on the free surface gives the desired displacements for an arbitrary distribution of pore pressure changes at depth.

$$u_i(\bar{x}) = \frac{1}{2\pi} \int_V dV_\xi \frac{1-2\nu}{\mu} \alpha p(\xi) \frac{x_i - \xi_i}{|\bar{x} - \xi|^3} \quad (\text{A.6})$$

Like the point source solution in a full-space, the displacements on the free surface from a point source in a half-space are purely radial. This solution assumes that the principle of superposition applies, which is a good approximation for the small volumetric strains expected in a reservoir being used for sequestration.

Eq. A.6 may also be found through the Mogi model. This model, used by Mogi to describe deformation induced by pressure changes in spherical magma chambers, applies to spherical sources of deformation in an elastic half-space having undergone a volume change ΔV . Deformation in the Mogi model is given by

$$\bar{u} = \frac{(1-\nu)}{\mu r^2} \sigma \quad (\text{A.7})$$

where r is the distance from the center of the spherical body to the point of deformation and σ is the deviatoric stress inducing deformation. In this model there is a non-unique relationship between volume change, stress, and the volume of the source. This relationship has the form

$$\Delta V = -\frac{\pi a^3}{\mu} \sigma \quad (\text{A.8})$$

where a is the radius of the spherical source. Poroelasticity (Biot, 1941 and 1956) gives us another relationship between the volume strain, deviatoric stress, and pore pressure change:

$$2\mu \varepsilon_{ij} = \sigma_{ij} - \frac{\nu}{1+\nu} \sigma_{kk} \delta_{ij} + \frac{1-2\nu}{1+\nu} \alpha p \delta_{ij} \quad (\text{A.9})$$

δ is the Dirac delta function and ε is deviatoric strain. Taking the sum of the principle strains (the trace of ε_{ij}) gives the volumetric strain on an element of rock,

$$\varepsilon_{kk} = \frac{3(1-2\nu)}{2(1+\nu)\mu} \left(\frac{\sigma_{kk}}{3} + \alpha p \right) \quad (\text{A.10})$$

Here σ_{kk} is the change in the internal (tensional) stress. By coupling with these poroelastic expressions we get a usable form of the Mogi source for our model

$$\bar{u}(r) = \frac{1-2\nu}{2\pi} \frac{\alpha p}{\mu} \frac{\hat{r}}{r^2} \delta V \quad (\text{A.11})$$

Integration of this expression yields Eq. A.6, the same result as the Green's Function solution using the same assumptions. Using this general result we are able to recover the more specific results used by Geertsma (1973), Yang (1988), and Segall (1992).

References

- Arts, R., Chadwick, A., Zweigel, P., van der Meer, L., Zinszner, B. (2002), *Monitoring of CO₂ Injected at Sleipner Using Time Lapse Seismic Data*, GHGT-6, Kyoto, Japan.
- Batzle, M., Wang, Z. (1992), *Seismic Properties of Pore Fluids*, Geophysics 57, 1396-1408.
- Berryman, J.G. (1988), *Seismic wave attenuation in fluid-saturated porous media*, Pageoph 128, 423-432.
- Biot, M.A. (1941), *General Theory of 3-Dimensional Consolidation*, J. Appl. Phys. 12, 155-164.
- Biot, M.A. (1956), *General solutions of the equations of elasticity and consolidation for a porous material*, J. Appl. Mech., 91-6.
- Bowers, G.L., (1995), *Pore Pressure estimation from Velocity Data: Accounting for Overpressure Mechanisms Besides Undercompaction*, SPE Drilling & Completion 10, 89-95.
- Eberhart-Phillips, D., Han, D-H., and Zoback, M. D. (1989), *Empirical relationships among seismic velocity, effective pressure, porosity, and clay content in sandstone*, Geophysics, 54, 82-89.
- Focke, J.W., and Munn D. (1987), *Cementation exponents in middle eastern carbonate reservoirs*, Soc. Pet. Eng., Form. Eval., 2, 155-167.
- Gassmann, F. (1951), *Über die elastizität poroser medien*, Vierteljahrsschrift der Naturforschenden Gesellschaft in Zurich, 96, 1-23.
- Geertsma, J. (1973), *Land subsidence above Compacting Oil and Gas Reservoirs*, J. Pet. Tech. 25, 734-744.
- Han, D. (1986), *Effects of porosity and clay content on acoustic properties of sandstones and unconsolidated sediments*, Ph.D. dissertation, Stanford Univ.
- Hoversten, G. M., Daily, T., Majer, E. (2001), *Crosswell Seismic and Electromagnetic Monitoring of CO₂ Sequestration*, AAPG annual meeting, Denver CO.
- Jackson, J.D. (1962), *Classical Electrodynamics*, John Wiley & Sons, Inc.
- Laine E.F. (1987), *Remote monitoring of the steam-flood enhanced oil recovery process*, Geophysics 52, 1457-1465.
- Latil, M. (1980), *Enhanced Oil Recovery*, Gulf Publishing Company.
- Lazaratos, S. K., and Marion, B. P. (1997), *Crosswell seismic imaging of reservoir changes caused by CO₂ injection*, The Leading Edge, Vol. 16., 1300-6.
- Maher, J.C., Carter, R.D. and Lantz, R.J. (1975), *Petroleum geology of Naval Petroleum Reserve No. 1, Elk Hills, Kern County, California*, USGS Professional Paper 912.
- Mavko, G., Mukerji, T. and Dvorkin, J. (1998), *The Rock Physics Handbook*, Cambridge University Press.
- McKenna, J., B. Gurevich, M. Urosevic, and B. Evans (2003), *Estimating bulk and shear moduli for shallow saline aquifers undergoing CO₂ injection*, SEGJ-Imaging Technology, Tokyo, Japan, 490-497.
- Mindlin, R. D., and Cheng, D.H. (1950), *Thermoelastic Stress in the Semi-infinite Solid*, J. Appl. Phys. 21, 931-933.

- Mogi, K. (1958), *Relations between the eruptions of various volcanoes and the deformations of the ground surfaces around them*, Bull. Earthquake Res. Inst. Tokyo, 36, 99-134.
- Moore, E.J., Szasz, S.E., Whitney, B.F. (1966), *Determining Formation Water Resistivity From Chemical Analysis*, JPT, March, 373-6.
- Moritis, G., ed. (1998), *EOR oil production up slightly*, Oil & Gas Journal 96, 49-77.
- Myer, L.R., G.M. Hoversten, and C.A. Doughty (2002), *Sensitivity and cost of monitoring geologic sequestration using geophysics*, GHGT-6, Kyoto, Japan.
- Nekut, A.G. (1995), *Crosswell electromagnetic tomography in steel-cased wells*, Geophysics 60, 912-920.
- Nolen-Hoeksema, R. C., Wang, Z., Harris, J. M., and Langan, R. T. (1995), *High-resolution crosswell imaging of a West Texas carbonate reservoir: Part 5: Core analysis*, Geophysics, 60, 712-726.
- Onn, F., Wynn, D.T., and Zebker, H.A. (2002), *On the Detectability of Ground Deformation for Monitoring CO₂ Sequestration in Underground Reservoirs Using InSAR and GPS*, Eos Trans. AGU, 83(47), Fall Meet. Suppl., Abstract G61B-0993.
- Orr, F. M. and Taber, J. J. (1984), *Use of carbon dioxide in enhanced oil recovery*, Science 224, 563-569.
- Pride, S.R., Harris, J.M., Johnson, D.L., Mateeva, A., Nihei, K.T., Nowack, R.L., Rector, J.W., Spetzler, H., Wu, R.S., Yamamoto, T., Berryman, J.G. and Fehler, M., 2003, *Permeability dependence of seismic amplitudes*, The Leading Edge, submitted.
- Reichle, D., Houghton, J., Kane, B., Ekmann, J. (1999), *Carbon Sequestration Research and Development*, U.S. Department of Energy Report.
- Rice, J.R., and Cleary, M.P. (1976), *Some Basic Stress Diffusion solutions for Fluid-saturated Elastic Porous Media with Compressible constituents*, Rev. Geophys. and Space Phys. 14, 227-241.
- SACS (2003), *Best Practice Manual*, Draft.
- Schlumberger (1985), *Schlumberger Log Interpretation Charts*, Schlumberger Well Services.
- Segall, P. (1992), *Induced Stresses due to Fluid Extraction from Axisymmetric Reservoirs*, Pageoph 139, 535-560.
- Spies, B.R., and Habashy, T.M. (1995), *Sensitivity analysis of crosswell electromagnetics*, Geophysics 60, 834-845.
- Torp, T.A., Gale, J. (2002), *Demonstrating Storage of CO₂ in Geological Reservoirs: the Sleipner and SACS Projects*, GHGT-6, Kyoto, Japan.
- Vargaftik, N.B. (1996), *Handbook of physical properties of liquids and gases : pure substances and mixtures*, Begell House.
- Vasco, D.W., Johnson, L.R., and Goldstein, N.E. (1988), *Using Surface Displacement and Strain Observations to Determine Deformation at Depth, With an Application to Long Valley Caldera, California*, J. Geophys. Res. 93, 3232-3242.
- Wang, G.C. (1982), *Microscopic investigation of CO₂ Flooding Process*, J. Pet. Tech. 34, 1789-1797.
- Wang, Z., and Nur, A. (1989), *Effects of CO₂ flooding on wave velocities in rocks with hydrocarbons*,

Soc. Petr. Eng. Res. Eng., 3, 429-439.

Wang, Z., Cates, M.E., and Langan, R.T. (1998), *Seismic monitoring of a CO₂ flood in a carbonate reservoir: a rock physics study*, Geophysics 63, 1604-17.

Wawersik, R. et al. (2001), *Terrestrial Sequestration of CO₂: An Assessment of Research Needs*, Advances in Geophysics, Vol. 43, 97-177.

Waxman, M.H. and Smits, L.J.M. (1968), *Electrical conductivities in oil-bearing shaly sands*, AIME Trans., 243, 107-122.

Wilt, M. J., Alumbaugh, D. L., Morrison, H. F., Becker, A., Lee, K. H., Deszcz-Pan, M. (1995), *Crosswell electromagnetic tomography; system design considerations and field results*, Geophysics 60, 871-885.

Wilt, M., Morrison, H. F., Becker, A., Tseng, H. W., Lee, K. H., Torres-Verdin, C. and Alumbaugh, D. (1995), *Crosshole electromagnetic tomography: A new technology for oil field characterization*, The Leading Edge, March, 173-177.

Wilt, M.J., and Alumbaugh, D.L. (1998), *Electromagnetic methods for development and production; state of the art*: The Leading Edge, April, 487-90.

Yang, X.M., Davis, P.M.; Dieterich, J.H. (1988), *Deformation from inflation of a dipping finite prolate spheroid in an elastic half-space as a model for volcanic stressing*, J. Geophys. Res. 93, no.5, 4249-4257.